2017-12-20

Optimal Control of Nonlinear Networks Dynamics with Applications to Brain Stimulation in Alzheimer's Disease

Sánchez Rodríguez, Lázaro Miguel

UNIVERSITY OF CALGARY

Optimal Control of Nonlinear Networks Dynamics with Applications to Brain Stimulation in Alzheimer's Disease

by

Lázaro Miguel Sánchez Rodríguez

A THESIS

SUBMITTED TO THE FACULTY OF GRADUATE STUDIES

IN PARTIAL FULFILMENT OF THE REQUIREMENTS FOR THE

DEGREE OF MASTER OF SCIENCE

GRADUATE PROGRAM IN BIOMEDICAL ENGINEERING

CALGARY, ALBERTA

DECEMBER, 2017

Abstract

Brain stimulation can modulate the activity of neural circuits impaired by Alzheimer's disease (AD), having promising clinical benefit. However, all individuals with the same condition currently receive identical brain stimulation, with limited theoretical basis for this generic approach. In this study, we introduce a control theory framework for obtaining exogenous signals that revert pathological electroencephalographic activity in AD at a minimal energetic cost, while reflecting patients' biological variability. By considering nonlinearities in our model, we identified regions for which control inputs fail to correct abnormal activity. We also found that limbic system and basal ganglia structures constitute the top target locations for stimulation in AD. Patients with highly integrated anatomical networks are the most suitable candidates for the propagation of stimuli and consequent success on the control task. Other diseases associated with alterations in brain dynamics and the self-control mechanisms of the brain can be addressed through our framework.

Acknowledgements

First and foremost, I would like to thank my supervisor, Dr. Roberto C. Sotero, for giving me the unique opportunity to join his lab and for his guidance and support throughout this path. My gratitude extends to the members of my supervisory committee, Dr. Oury Monchi and Dr. Nils Forkert, as well. Their suggestions and feedback enriched my initial proposal and its realization. I am also grateful to the Biomedical Engineering Graduate Program and the CREATE i3t Program for providing the funding for this project. Thank you.

Many people are directly linked to the preparation of this thesis. I would like to acknowledge them in what follows. Dr. Jeff Pieper was a reference for approaching the Riccati equation control theory. Dr. Doug Phillips assisted with using University of Calgary's computing clusters. My lab mates, especially Mehdy Dousty, have been a wonderful source of feedback. Erica Baines, Marta Pietrzak, Aralia Leon, Nikhil Amin and Maribel Perry read the manuscript and made valuable recommendations for its improvement. My deepest gratitude to Dr. Yasser Iturria-Medina for granting me access to the processed diffusion data. The Alzheimer's Disease Neuroimaging Initiative recorded the data that was used in this work.

Finally, I must go to the foundations and acknowledge the influence that Dr. Pedro Valdes, Dr. Jorge Bosch, Dr. Jorge Riera and Dr. Juan C. Jimenez, from the Cuban Neuroscience Center, had on my interest in computational neuroscience and biomedical engineering. There is a vast worldwide network of authentic friends that constantly push me beyond known limits. My family, both in Cuba and the United States, are the pillar for everything I am and have accomplished. Among them, my uncle Maxi and my cousin Rodney feed my scientific curiosity.

Table of Contents

List of Tables

List of Figures and Illustrations

List of Symbols, Abbreviations, Nomenclatures

Symbol	*Definition*
AD	Alzheimer's disease
aDBS	Adaptive deep brain stimulation
ADNI	Alzheimer's Disease Neuroimaging Initiative
APOE e4	Apolipoprotein e4 allele
CSF	Cerebrospinal fluid
DBS	Deep brain stimulation
DW-MRI	Diffusion weighted magnetic resonance imaging
EEG	Electroencephalogram, electroencephalographic activity
F	F-statistic
FDA	Food and Drug Administration
HARDI	High angular resolution diffusion imaging
LFP	Local field potential
lqr.m	MATLAB function for solving the linear quadratic regulator
MNI	Montreal Neurological Institute (coordinate system)
MRI	Magnetic resonance imaging
n	Number of elements in the sample (statistics)
NLduff_ADNI_hd_subject.m	MATLAB function for computing the control signals
ODF	Intravoxel fiber distribution
P	P-value
pref.m	MATLAB function for generating scale-free networks
r	Pearson correlation coefficient
s.e.m	Standard error of the mean
SF	Scale-free network
SPM	Statistical Parametric Mapping
SW	Small-world network
tDCS	Transcranial direct current stimulation
TMS	Transcranial magnetic stimulation

WattsStrogatz.m	MATLAB function for generating small-world networks
$\mathbb{R}^n$	The *n*-dimensional real space
C^m	The set of functions with continuous derivatives up to m
E_g	Network global efficiency
M_i	Node communicability
W_{ji}	Anatomical connection density between regions i and j
b_i	Node betweenness centrality
c_i	Node clustering coefficient
e_i	Node eccentricity
e_{xi}	The i −th difference of the observable variables
l_{ji}^{ω}	Shortest weighted path length between nodes i and j
q_i	Node closeness centrality
s_i	Node strength
$\boldsymbol{a}^T$	Transpose of $\boldsymbol{a}$
$\boldsymbol{e}_0$	Initial conditions for the state vector
$\boldsymbol{z}_1$	Solution to the Duffing system for a set 1 of parameters. Later identified as 'pathological solution'
$\boldsymbol{z}_2$	Solution to the Duffing system for a set 2 of parameters. Later identified as 'healthy solution'
~	Approximately
×	Times (for matrix dimensions)
∈	Element of
$\mathbb{R}$	The set of real numbers
Γ	Set of edges in a network
Δ	Set of nodes in a network
C	Network average clustering coefficient
D	Network diameter
G	Network, graph
Hz	Hertz
J	Cost index, energy function

N	Number of nodes in a network
$P(k)$	Degree probability
TR	Time-to-repeat (MRI)
V	Volts
b	Strength of the magnetic diffusion gradient, b-value
d	Number of links on arrival given in a SF network.
	Number of neighboring connections in a SW network
k	Degree of a node
l	Network characteristic path length
mV	Millivolts
mm	Millimetres
n	Number of state variables in the dynamical system
r	Network radius
s	Seconds
t	Time
$u(t)$	Input (control) signal
v	Stable state that counts for state-independent terms
$\boldsymbol{A}(\boldsymbol{e})$	Apparent linearization matrix
$\boldsymbol{B}$	Input vector
$\boldsymbol{I}$	Identity matrix
$\boldsymbol{Q}$	Weight for the influence the state vector has in the cost
$\boldsymbol{R}$	Weight for the influence the control signal has in the cost
$\boldsymbol{S}(\boldsymbol{e})$	Solution to the state-dependent Riccati equation
$\boldsymbol{W}$	Anatomical connection density matrix
$\boldsymbol{e}$	State vector.
	Difference between two solutions of the Duffing system
$\boldsymbol{f}(\boldsymbol{e})$	System function
$\boldsymbol{x}$	Observable variables (excitatory postsynaptic potentials)
$\boldsymbol{y}$	Derivative of the observable variables
$\boldsymbol{z}$	State variable in the Duffing system

α	Time constant
β	Strength of the coupling
γ	Strength of the nonlinearity
ρ	Spearman's rank correlation coefficient
σ	Probability of rewiring a link in a SW network
$\mathbf{0}$	Matrix of zeros
$\mathbf{1}$	Matrix of ones

Chapter One: **Introduction**

1.1 Brain stimulation

Since the late 1970's, brain stimulation has been researched and applied for the treatment of several neurological and psychiatric disorders[1–3], including epilepsy, stroke, schizophrenia, Parkinson's disease, major depressive disorder and Alzheimer's disease. Overall, stimulation consists in exciting neuronal populations by sending exogenous signals to specific targets in the brain. Amidst the most widely used brain stimulation techniques are transcranial magnetic stimulation (TMS)[4], transcranial direct current stimulation (tDCS)[5], and deep brain stimulation (DBS)[6]. A general, schematic representation illustrating the use of these brain stimulation technologies is shown in Figure 1-1. Current brain stimulation techniques differ in reach, design and degree of invasiveness. For example, electric signals are used in tDCS and DBS, whereas TMS employs magnetic inputs. In DBS, a device is inserted into the patient's organism to produce electrical impulses, allowing the stimulation of subcortical structures. On the other hand, cortical structures are excited by means of TMS and tDCS. The use of one or the other technique for the treatment of a given clinical condition depends mainly on the mechanisms associated with the disorder and the understanding the researcher/clinician has on how to influence these mechanisms.

In effect, brain stimulation aims to produce long-term corrections of pathological activity by steering (controlling) it towards a trajectory (pattern of brain activity) that is considered healthy. However, stimulation treatments are currently identical for all individuals with the same clinical condition[2–6], disregarding biological variability which makes individuals display the signs of a disease and respond to therapies in different ways. Consequently, presently used stimulation therapies have limited success rates. Additionally, brain stimulation protocols are likely

suboptimal in their selection of the signal shape, amplitude, and stimulation sites, since they are set by trial-and-error. By optimal, we mean inputs that make the pathological state disappear while the energy used by the external controlling agent (cost) is minimal. A simplistic illustration of a DBS signal and the definition of the currently used stimulation parameters appear in Figure 1-2.

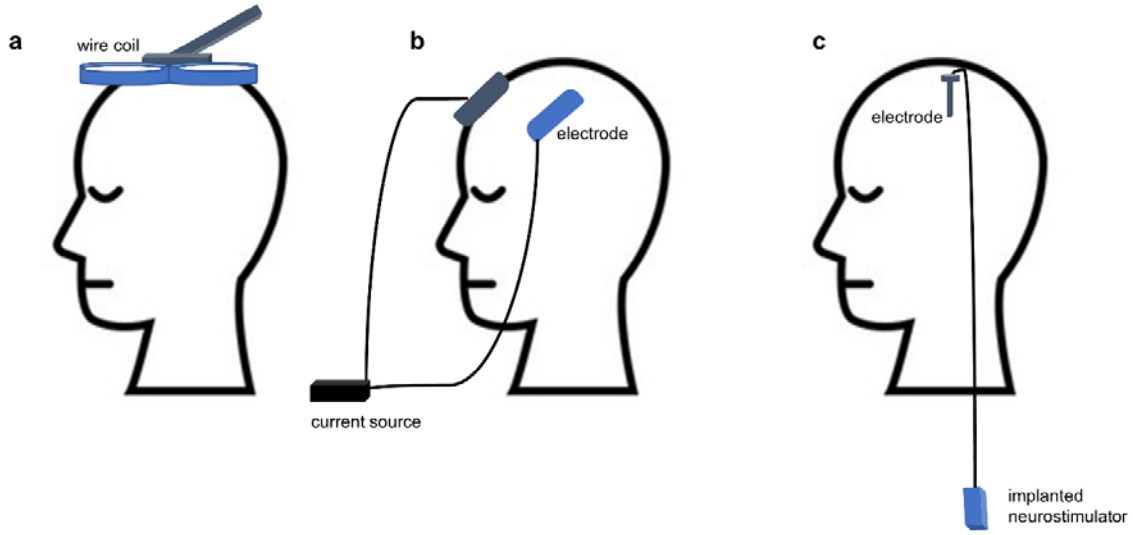

Figure 1-1: **Schematic representation for the application of brain stimulation. a**) Transcranial magnetic stimulation (TMS). A focused magnetic field delivered by a wire coil excites neuronal circuits in the cortical area under the coil placement, causing long-term changes to brain activity[4]. **b**) Transcranial direct current stimulation (tDCS). A weak, direct current is applied to the brain via electrodes over the scalp, to increase or decrease excitability in selected areas. The distribution of current flow and the intensity of stimulation over the brain can be tuned by adjusting the location of the electrodes[5]. **c**) Deep brain stimulation (DBS). Unlike TMS and tDCS, DBS requires the surgical implantation of a device (the neurostimulator), which sends electrical impulses through – also implanted– electrodes, to certain brain targets. This can modulate the pathological oscillatory activity between brain regions[6,88]. Several treatments using these technologies are approved by the Food and Drug Administration (FDA)[1] and currently applied within different health systems.

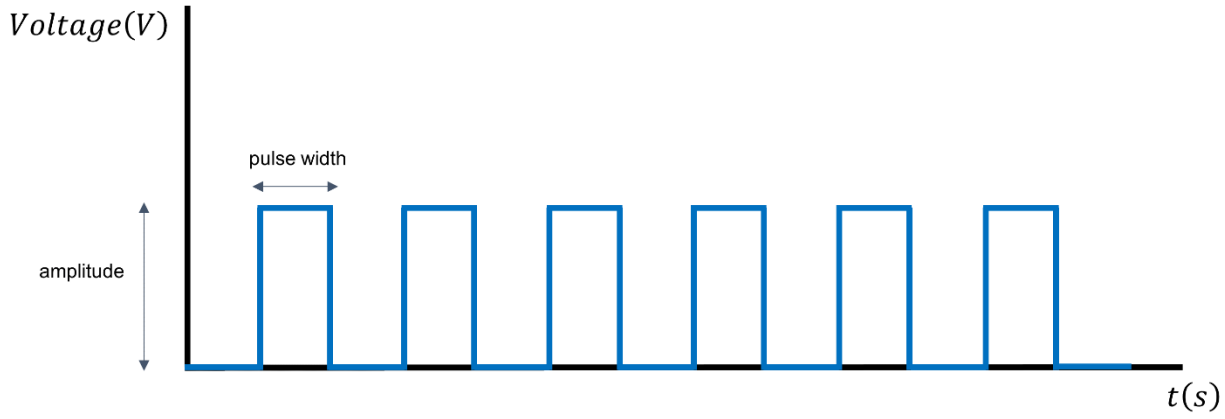

Figure 1-2: **Representation of a deep brain stimulation signal**. Continuous stimulation is delivered in the shape of pulses with defined amplitude and width. The number of pulses per second can also be adjusted. For example, Lozano et al.[3] chose a 3.0–3.5 V stimulation, with a 90 microseconds pulse width and a rate of 130 Hz.

1.2 Modeling the control of brain networks

To address some of the above-mentioned issues regarding brain stimulation, computational modeling techniques have been previously used[1,7–9]. However, modeling brain stimulation requires the consideration of some known facts, such as the evolution of brain activity being intrinsically related to the subjacent anatomical network, and the interplay of various neuronal populations[10]. A network is usually represented as a graph in which the nodes correspond to the elements and the edges symbolize the existence of a connection (interaction) between elements[11]. As reported by several studies, both functional networks (given by the statistical dependencies between remote neurophysiological events) and effective connectivity (activity-dependent influences that a neural system exerts over another)[12] correlate to the structural connections between conglomerates of neurons[13,14], which are customarily computed from diffusion weighted magnetic resonance images

(DW-MRI). As in any other network, it is reasonable to assume some elements (or nodes) have an architectural leading role in the self-regulation of that neural system[15,16]. An input feeding into one of these elements has the potential to propagate through the network, influencing the system towards the state desired by the controller.

The existence and characteristics of such input signals is then given by the dynamical structure of the system and the way its elements are coupled to the inputs. Systems in which those signals exist are known as controllable (as opposed to uncontrollable), relating to the property 'controllability'[17]. In the simple network in Figure 1-3a, a stimulus entering the element marked as '1' would propagate and reach all the other nodes. In this case, the solution to the system is unique for each stimulus, independently of the detailed values of the couplings between the state variables, and the states and the controller. This system is controllable. Nevertheless, this does not hold for the network in Figure 1-3b: an input to node '1' can never completely control the network because the existing structural couplings always yield the same dynamics (Figure 1-3c). Some studies have focused on identifying the most suitable sites for network controllability from a structural viewpoint only[18] while simplifying the dynamical interactions occurring on top of the connectivity scaffold.

Other studies[1,7–9] used linear dynamics to model neural processes. However, most of the brain phenomena are known to be intrinsically nonlinear[10,19–22]. For example, the electrical activity of the brain, as recorded in the electroencephalogram (EEG), and its switching between dynamical states[21] cannot be explained otherwise. As stated before, the effect of stimulation signals is indeed converting pathological dynamics into a healthy pattern of brain activity. Hence, the predictions on neural network control obtained from linear dynamics should be taken with caution. Neglecting

the nonlinear nature of the brain for the sake of mathematical simplicity might bias or corrupt the results therein obtained.

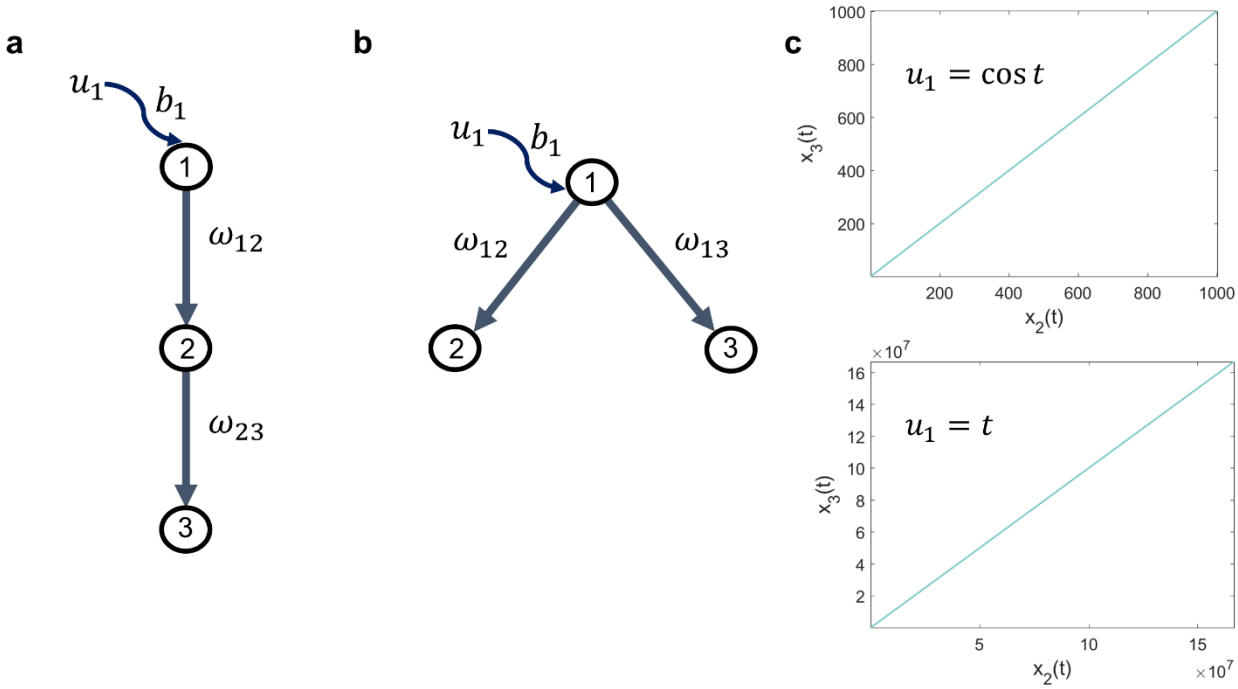

Figure 1-3: **The notion of controllability. a**) The states associated with nodes '1', '2' and '3' are uniquely determined by the input signal $u_1(t)$ in the way the elements are connected. The linear system is controllable. The input to node '1' reaches the subsequent nodes in the path and conditions their activity. **b**) The system is uncontrollable by stimulating node '1' only, no matter how we tune the connectivity parameters. **c**) A linear system mounted over the network represented in **b** will always get stuck in the plane $\omega_{12}x_3(t) = \omega_{13}x_2(t)$ in the state space. This is shown for two different inputs that '1' receives ($\omega_{12} = \omega_{13} = b_1 = 1$, for simplicity). Panels **a** and **b** are adapted from Liu et al.[89]. Examples of networks in which only a certain combination of the couplings yields uncontrollable systems can be found therein. See Chapter 2 for further details on network theory and the notion of controllability.

Finally, the identification of optimal (electromagnetic) signals among the many that can be created[4–6] has a paramount importance in terms of patient's welfare and technological improvement. As such, modeling approaches should be able to predict the brain structures that better respond to targeted stimulation for achieving a control objective over the network. For instance, the surgical implantation of devices (for DBS) could be avoided if theoretical calculations envisage that stimulation of cortical neuronal conglomerates, with, e.g., tDCS, produces comparable results to what is achieved by means of DBS. In the same way, pinpointing optimal control signals likely translates to less exposure for the patient and to a reduction of procedure-related costs in terms of number of sessions required, the shape and amplitude of the signals that are used, etc.

1.3 Alzheimer's disease

Deep brain stimulation for Alzheimer's disease (AD) is in clinical trial with promising results[2,3]. AD is a neurodegenerative disease that is diagnosed when cognitive impairment and behavioral derangement affect activities of daily living[23]. As of 2016, it affected 47 million people worldwide according to Alzheimer's Disease International[24]. The Alzheimer Society of Canada reported the costs of dementia as $10.4 billion annually[24]. Because of the complex mechanisms and non-physiological factors that interact in an intricate manner[25], our understanding of the disease and our ability to produce efficient therapeutic interventions has been limited. The relatively recent progress achieved in medical imaging has contributed to find quantitative measures for AD and to gain insight into the cascade of cognitive/clinical events leading to it[25,26]. Classic biomarkers of AD include vascular and glucose metabolism dysregulation, amyloid-β and tau deposition, white matter degeneration, functional impairment, and grey matter atrophy[26].

One of the signatures of AD is its slowing down of the EEG (i.e. contains more low-frequency power). An increase of power in the theta band (4.0-7.5 Hz) of the EEG spectrum, and a decrease of power in the alpha (8.0-12.5 Hz) and beta (13.0-32.0 Hz) bands[27,28] were found in AD. As reported by several studies, there is a correlation between cognitive impairment and the acuteness of EEG abnormalities[29,30]. Patients with stable EEG during a one-year follow up showed slower decline in praxic functions and a lower risk of institutionalization than AD patients with slower EEG[29]. Additionally, the use of cholinergic drugs (which can transiently shift the EEG spectra towards normality) was related to improved memory and attention performances in AD[29,31]. On the other hand, anatomical networks obtained from DW-MRI show abnormalities in AD[16,32,33]. Among these irregularities appear a decreased global efficiency for the transmission of information and an increase in the average distance from one node to any other in the network. Both these abnormalities affect the small-worldness property[34] of the anatomical networks, which assures that most nodes can be reached from every other node by a small number of steps. Human brain anatomical networks are also considered scale-free[15], with some nodes having many more connections than the rest, for achieving robustness to failure.

On the other hand, several attempts have been made to assess the potential brain stimulation has for treating AD[35]. Only DBS of the fornix has recently passed phase II trials[2,3]. Reversion of impaired glucose metabolism in the temporal and parietal association cortices along with slowing of cognitive indicators for the progression of AD confirmed the therapeutic effect of DBS. The stimulation protocol in these studies was set up according to previous experience the researchers had in the use of DBS treatments for Parkinson's disease. However, unlike the case of Parkinson's where a decrease in tremor constitutes a short-term measure for the success of the therapy, these

AD studies lacked such a biomarker. Consequently, they were unable to guarantee that the stimulation parameters were the optimal ones for their purposes. Additionally, only participants aged ≥ 65 years reported benefit. The results of the commented research highlight the need for clarifying the neural mechanisms of positive effects induced by stimulation and understanding ways of personalizing the application of stimulation protocols.

1.4 Synthesis and rationale

A review of the literature pertaining to brain stimulation and its recent application to AD as summarized in the previous sections reveals the existence of the following issues:

1) Currently used brain stimulation treatments lack knowledge of the selection of target locations, of the generation of signals for correcting pathological activity and of how both these parameters relate to optimal signal propagation over the brain network. Additionally, patients respond differently to identical stimulation treatments, seemingly a consequence of biological variability.
2) Previous modeling approaches for stimulation have overlooked the nonlinear dynamical nature of the brain. They only partially solve, or do not solve the knowledge gaps stated in (1) whatsoever.

Given the accelerated pace at which brain stimulation is being found as a safe long-term corrector of pathological activity, a proper framework that clarifies its underlying operative principles is necessary.

1.5 A solution for optimal nonlinear network control

There is a mathematical tool that deals with nonlinearities while optimizing input signals for controlling nonlinear dynamical systems. It is known as the State-Dependent Ricatti Equation

algorithm (SDRE)[36–38]. Any nonlinear dynamical system can be written, under some conditions, as a linear system in which the matrix for the interactions between the state variables is dependent on the states themselves (see Section 2.2.2 for further details). SDRE takes advantage of this abstraction and applies the robust linear optimal control theory[17] to (locally) linear systems at each time instant, while solving for the feedback signal that controls the nonlinear system at the lowest possible energetic cost.

SDRE has a vast set of applications in mechanical problems and aerospace engineering though few in the fields of biological and high-dimensional systems, where the above-mentioned simplistic linear approaches have been preferred. Such an application of SDRE could reconcile the theory of neural network control and the true nonlinear nature of the brain. It can also shed light on the development of efficient stimulation therapies for AD. Consequently, *we propose the development of a SDRE-based framework for searching optimal exogenous signals to control nonlinear brain networks in AD*.

1.6 Hypothesis and specific objectives

1.6.1 Hypothesis

The SDRE-control of realistic brain networks provides a theoretical framework for the optimal implementation of brain stimulation techniques in AD.

1.6.2 Specific objectives

Objective 1: To develop the modeling framework for obtaining optimal control signals that steer pathological brain activity to healthy activity.

Objective 2: To investigate different scenarios for optimally controlling networks with nonlinear dynamics. To accomplish this goal, exploratory control of oscillatory dynamics over synthetic scale-free and small-world networks will be performed.

Objectives 1 and 2 pertain to a wider scope of this work. Several combinations of diseases and stimulation scenarios could be addressed by developing the framework alone. In effect, given any two trajectories, the application of the optimal control signals synchronizes one trajectory with the other. The analysis of such control inputs not only informs about therapies for a pathology, but can also be used to study healthy self-regulatory mechanisms in the brain. Therefore, trying the framework on network models provides insights into efficient optimal strategies (we would expect that the 'better connected' a node is in the network, the 'easier' is to control the network while stimulating it, for example). This thesis focuses on brain stimulation of AD given its tentative favorable impact to society, especially in healthy aging.

Objective 3: To apply the SDRE-framework to the modeling of brain stimulation in Alzheimer's disease. To accomplish this goal, we will:

3.1- Define a dynamical system that mimics experimentally recorded EEG activity at the disease and in health.

3.2- Use anatomical connection graphs obtained from individual DW-MRI data in AD as the scaffold for the interactions in the dynamical model.

3.3- Obtain the signals that –placed over different brain regions– can steer the pathological state to the healthy one in an optimal way, *for each subject*.

Objective 4: To characterize the optimal control signals obtained in Objective 3, in terms of network topology and cognitive-physiological implications.

Objective 5: To explore the parameter space and study the effect of the model parameters in the characteristics of the control signals.

1.7 Structure

The rest of this thesis is organized as follows. In Chapter 2, the body of theory to be used is presented. This includes important concepts in network theory, the notions of optimal control and nonlinear optimal control, and the numerical methods and tools used to solve the control problem. Additionally, a description of the data used in the study, and the processing they previously underwent, is included. Chapter 3 contains the original material in this thesis. First, the modeling framework for obtaining optimal control signals that steer pathological brain activity to healthy activity is introduced. Results over synthetic scale-free and small-world networks constitute the preamble to the analysis of controlling the AD network. The optimal inputs to steer pathological AD activity towards a healthy state, the differences between linear and nonlinear modeling and the effects of the topology in the results are characterized in the last section of Chapter 3. In Chapter 4, we discuss the obtained results, mostly in terms of the relevance they have for AD and how they relate to the brain's function and anatomy, how to implement the delivery of our signals and the limitations that our solution presents hitherto. Finally, the main MATLAB code we used to generate the optimal control signals is attached as an appendix to this thesis.

Chapter Two: **Methods**

2.1 Connectivity networks

A network is usually represented as a graph in which the nodes correspond to the elements and the edges symbolize the existence of an interaction between elements. Overall, the network is characterized by a set of N nodes, Δ, and a set of edges, Γ: $G = [\Delta, \Gamma]$. If, additionally the edges take values other than 0 (no connection) and 1 (a connection exists), the network is said to be weighted and the values of the weight contain information about the connection strengths. The links can also be directed. However, current neuroimaging methods fail to detect anatomical or effective directionality[11]. Consequently, all the networks in this thesis are undirected (their matrix representation is symmetric).

2.1.1 Scale-free networks

The Barabási and Albert's model[39] (or "richer gets richer") assumes that new nodes in a network are not connected at random but with high probability to those which already possess a large number of connections (have large degree). These nodes with large degree, also known as hubs, are thought to be key for the functioning of the network. The degree probability is the probability, $P(k)$, that a node in the network interacts with k other nodes. In the Barabási and Albert's model, $P(k)$ decays as a power law, which conduces to scale-invariance. Examples of the so-called scale-free (SF) networks are the World Wide Web, actors' collaboration and airports networks. In the brain, there is preferential attachment to hubs[15] as well, which is thought to be a consequence of optimization during evolution.

We generate SF networks by using MATLAB's toolbox CONTEST[40]. CONTEST's function *pref.m* uses the algorithm proposed by Batagelj and Brandes[41]. Thus, $pref(N, d)$ creates

a N −dimensional SF network in which each node is given d links on arrival. For sufficiently big networks, the mean degree is approximately $2d$. Figure 2-1a shows a SF network with $N = 78$ and $d = 4$.

2.1.2 Small-world networks

In 1998, Watts and Strogatz[34] found that many real-world networks are highly clustered like regular graphs –where each node has the same number of neighbors– yet have small average distance between nodes, like a random graph. This assures that most nodes can be reached from every other node by a small number of steps. Thus, the Watts and Strogatz model (SW) resembles the small-world phenomenon found in social networks: "we are all linked by a short chain of acquaintances". Anatomical brain networks present small-world attributes for achieving efficiency in local and global communication[15].

We generate SW networks by using MATLAB's function *WattsStrogatz.m.* The algorithm for generating a N −dimensional SW network, starts by connecting each of the nodes to its d nearest neighbours on each side. Then, with probability σ, each edge in the graph is rewired to a node chosen at random. Figure 2-1b shows a SW network created with $N = 78$, $d = 4$ and $\sigma = 0.1$.

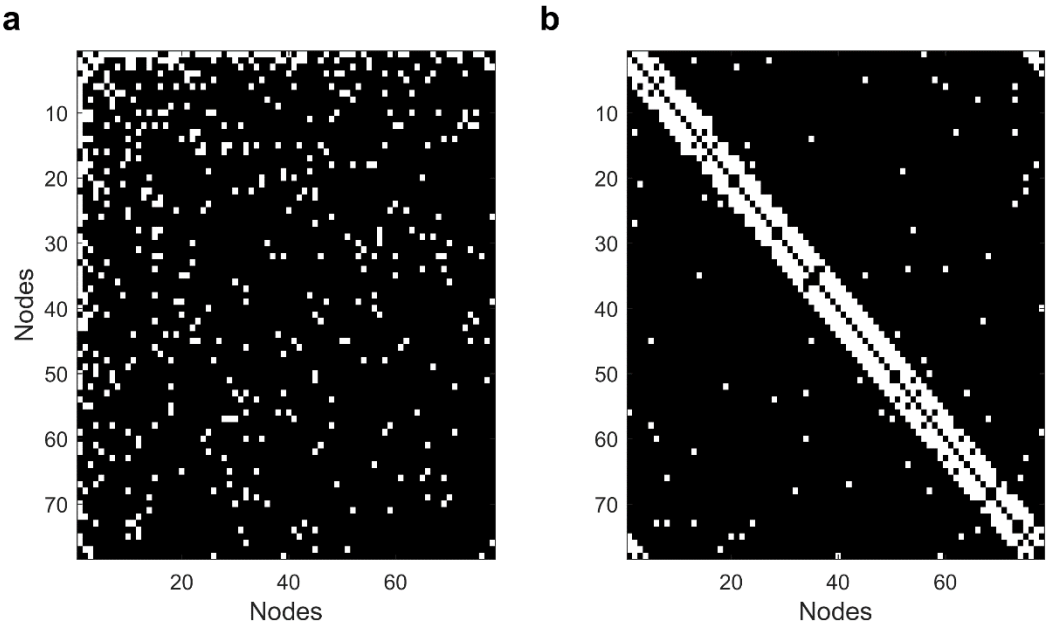

Figure 2-1: **Example of connectivity matrices in network models. a**) Scale-free network ($N = 78,\ d = 4$). **b**) Small-world network ($N = 78,\ d = 4,\ \sigma = 0.1$). The white squares denote the existence of a connection.

2.1.3 Alzheimer's anatomical networks

2.1.3.1 Study participants

This study uses 41 individual baseline data from the Alzheimer's Disease Neuroimaging Initiative (ADNI). Structural magnetic resonance images (MRI) and diffusion weighted MRI (DW-MRI) were acquired for each of the ADNI subjects included in the study. We use the individual clinical diagnoses assigned by the ADNI experts, which were based on multiple clinical evaluations. The 41 subjects were diagnosed as Alzheimer's patients. The ADNI was launched in 2003 as a public-private partnership, led by Principal Investigator Michael W. Weiner, MD. The primary goal of ADNI has been to test whether serial magnetic resonance imaging, positron

emission tomography, other biological markers, and clinical and neuropsychological assessment can be combined to measure the progression of mild cognitive impairment and early AD.

See Table 2-1 for demographic characteristics of the included ADNI subjects. Data appears as mean (standard deviation) or number of subjects (percentage).

Table 2-1: **Demographic characteristics of the 41 ADNI subjects included in the study**

Characteristic	Females	Age(years)	Education(years)	APOE e4 (1 copy)	APOE e4 (2 copies)
Values (41 AD-patients)	14(34.1)	75.6(8.0)	15.3(3.0)	20(48.7)	5(12.2)

2.1.3.2 Ethics statement

The study was conducted according to Good Clinical Practice guidelines, the Declaration of Helsinki Principles, US 21CFR Part 50—Protection of Human Subjects, and Part 56—Institutional Review Boards, and pursuant to state and federal HIPAA regulations (adni.loni.usc.edu). Study subjects and/or authorized representatives gave written informed consent at the time of enrolment for sample collection and completed questionnaires approved by each participating sites Institutional Review Board. The author obtained approval from the ADNI Data Sharing and Publications Committee for data use and publication, see documents http://adni.loni.usc.edu/wp-content/uploads/how_to_apply/ADNI_Data_Use_Agreement.pdf and http://adni.loni.usc.edu/wp-content/uploads/how_to_apply/ADNI_Manuscript_Citations.pdf, respectively.

2.1.3.3 Data acquisition and processing

2.1.3.3.1 Disclaimer

ADNI collected the data used in this study. All data is anonymous and available from ADNI's database (adni.loni.usc.edu). As such, the investigators within the ADNI contributed to the design and implementation of ADNI and/or provided data but did not participate in analysis or writing of this thesis. A complete listing of ADNI investigators can be found at: http://adni.loni.usc.edu/wp-content/uploads/how_to_apply/ADNI_Acknowledgement_List.pdf. Dr. Yasser Iturria-Medina at the Montreal Neurological Institute and Hospital processed the magnetic resonance images from ADNI. We acknowledge Dr. Iturria-Medina for granting us access to the processed data. Dr. Iturria-Medina did not participate in any other stage of the study.

2.1.3.3.2 Structural MRI

Brain structural T1-weighted 3D images were acquired for all subjects. For a detailed description of acquisition details, see http://adni.loni.usc.edu/methods/documents/mri-protocols/. All images underwent non-uniformity correction using the N3 algorithm[42]. Next, they were segmented into grey matter, white matter and cerebrospinal fluid (CSF) probabilistic maps, using SPM12 (www. fil.ion.ucl.ac.uk/spm). Grey matter segmentations were standardized to MNI space[43] using the DARTEL tool[44]. Each map was modulated to preserve the total amount of signal/tissue. Mean grey matter density and determinant of the Jacobian (DJ)[44] values were calculated for 78 regions covering all the brain's grey matter[45].

2.1.3.3.3 Diffusion weighted MRI

High angular resolution diffusion imaging (HARDI) data was acquired for 41 subjects. For each diffusion scan, 46 separate images were acquired, including 5 b_0 images (no diffusion sensitization) and 41 diffusion-weighted images ($b = 1000\, s\, mm^{-2}$). Other acquisition parameters were: 256×256 matrix, voxel size: $2.7 \times 2.7 \times 2.7\, mm^3$, $TR = 9000\, ms$, 52

contiguous axial slices, and scan time, $9\ min$. ADNI aligned all raw volumes to the average b_0 image, corrected head motion and eddy current distortion.

2.1.3.3.4 Anatomical networks

The T1-weighted 3D anatomical images were registered to the b_0 images using a normalized mutual information method[46]. Probabilistic axonal connectivity values between each brain voxel and the surface of each considered gray matter region (voxel-region connectivity) were estimated using a fully automated fiber tractography algorithm[47] and the intravoxel fiber distributions (ODFs) of 41 diseased subjects from ADNI. ODF reconstructions were based on Spherical Deconvolution[48]. A maximum of $500\ mm$ trace length and a curvature threshold of $\pm 90°$ were imposed as tracking parameters. Based on the resulting voxel-region connectivity maps, the individual region-region anatomical connection density matrices[47], $\boldsymbol{W}$, were calculated. For any subject and pair of regions i and j, the W_{ji} measure ($0 \leq W_{ji} \leq 1, W_{ji} = W_{ij}$) reflects the fraction of the region's surface involved in the axonal connection with respect to the total surface of both regions. A network backbone, containing the dominant connections in the average network, was computed using a minimum-spanning-tree based algorithm[11] and used as a mask for all the subjects' connection maps. Visualization of the anatomical networks was partially performed by means of BrainNet Viewer[49]. The connectivity matrices corresponding to two subjects in ADNI's database are shown in Figure 2-2 as an illustrative example.

The anatomical connection densities constitute a normalization to the number of "effective" voxels involved in a connection[47], obtained from dividing it by the total number of superficial voxels of the two areas. Effective voxels are counted according to their maximum probability of being connected to the voxels in the surface of the second area. This magnitude alone provides an

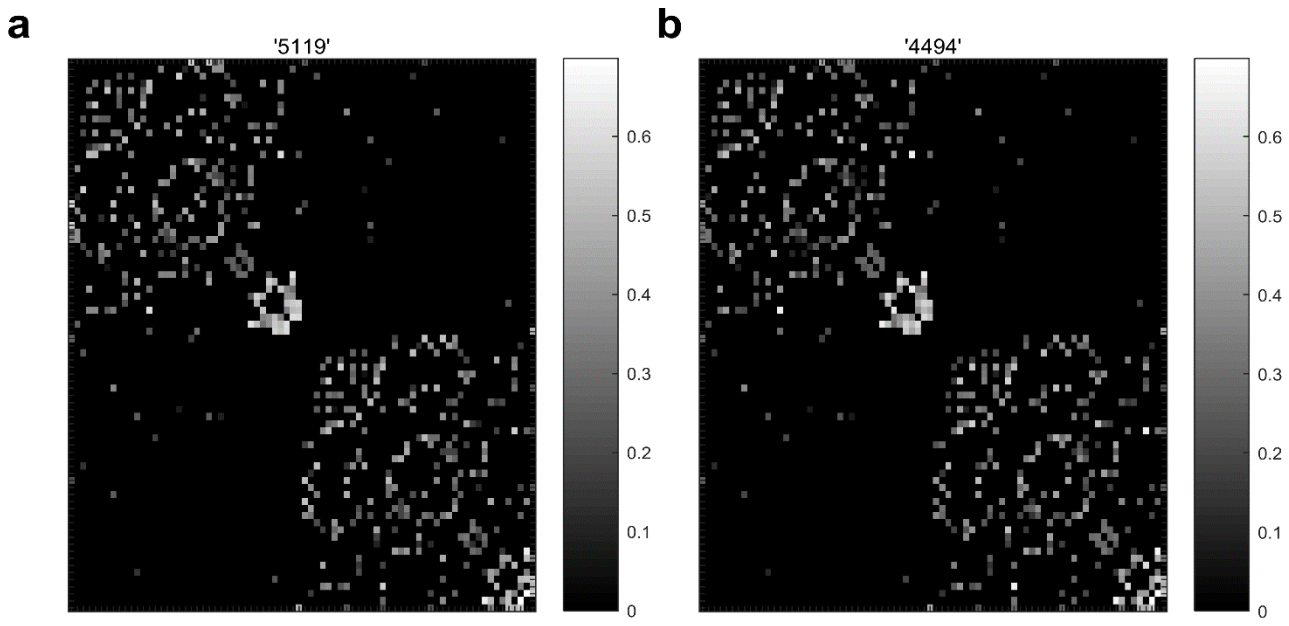

Figure 2-2: **Anatomical connectivity matrices**. **a**) Corresponds to the ADNI subject identified as '5119'. **b**) Corresponds to the ADNI subject identified as '4494'. The grey-scale represents the strength (weight) of a connection. Non-dominant connections are assigned a null weight[11]. Brain regions[45] appear in the following order, starting by the left hemisphere: caudal anterior cingulate, caudal middle frontal, cuneus, entorhinal, fusiform, inferior parietal, inferior temporal, isthmus cingulate, lateral occipital, lateral orbitofrontal, lingual, medial orbitofrontal, middle temporal, parahippocampal, paracentral, pars opercularis, pars orbitalis, pars triangularis, pericalcarine, postcentral, posterior cingulate, precentral, precuneus, rostral anterior cingulate, rostral middle frontal, superior frontal, superior parietal, superior temporal, supramarginal, transverse temporal, insula, accumbens area, amygdala, basal forebrain, caudate, hippocampus, pallidum, putamen and thalamus proper.

estimation of the potential information flow between any pair of regions and is proportional to the number of nervous fibers shared by these regions[15]. The further computation of the connection densities allows to know if a pair of regions has more or less connection density than another pair of regions with a different or equal number of superficial voxels[15]. For example, two regions of interest can present a high value of anatomical connection density if they contain a small number of superficial voxels (each voxel having an anatomical connectivity value close to 1 with the surface of the other zone)[47]. The anatomical networks based on connection densities were previously used in a study on multifactorial AD's progression[25].

2.1.4 Topological measures

Several quantities characterize the connectivity profiles of the elements and networks altogether. In this section, we briefly define the measures we use in this work. These measures are obtained by means of the Brain Connectivity Toolbox[11]. The quantities herein used are (generally) weighted[15,50] since the anatomical connection densities can take any value from 0 to 1. A weight, W_{ji}, represents the fraction of a region's surface involved in the axonal connection with respect to the total surface of both regions, i and j. We assume that the physical length of an edge connecting i and j is inversely proportional to W_{ji} (areas with high connectivities are physically closer)[15]. Thus, the shortest weighted path length between any two nodes in the graph, l_{ji}^{ω}, is their shortest weighted (geodesic) distance[11].

On the contrary, the synthetic network models are binary graphs. In the calculation of the topological measures for the SF and SW networks, the quantities below are modified so that all the weights are 1 if a connection exists. In binary networks, the sum of the weights for the

connections a node has, known as 'strength' (see below), reduces to its number of links, which is conventionally called 'degree'. The rest of the quantities are called likewise.

2.1.4.1 Local measures

Important nodes in a network often participate in a high number of connections with other elements of the network. Most of the widely used local measures quantify the degree of centrality based on the idea that important nodes are involved in many short paths and have a key role for information flow in the network[11]. Other measures, like communicability[9,51], account not only for the shortest path lengths communicating two nodes in a network, but also for indirect multiple connections that permit information to travel.

List of local measures:

Strength (s_i): the sum of the weights of the edges connected to node i:

$$s_i = \sum_{j \in \mathrm{G}} W_{ji}$$

Eccentricity (e_i): the maximal shortest path length between node i and any other node in the graph:

$$e_i = \max_{j \in \mathrm{G}, j \neq i} l_{ji}^{\omega}$$

Closeness centrality (q_i): the average distance between node *i* and every other node in the graph:

$$q_i = \frac{N-1}{\sum_{j \in \mathrm{G}, j \neq i} l_{ji}^{\omega}}$$

Betweenness centrality (b_i): the fraction of all shortest paths in the network that contain node i:

$$b_i = \frac{1}{(N-1)(N-2)} \sum_{\substack{h,j \in \mathrm{G} \\ h \neq j \neq i}} \frac{\sigma_{hj}(i)}{\sigma_{hj}}$$

σ_{hj} is the total number of paths from h to j and $\sigma_{hj}(i)$ is the number of these paths passing through node i.

Clustering coefficient (c_i): the fraction of triangles around node i:

$$c_i = \frac{2t_i^{\omega}}{k_i(k_i - 1)}$$

k_i is the degree of node i (total number of edges connected to it) and t_i^{ω} is the weighted geometric mean of triangles around i, $t_i^{\omega} = \frac{1}{2}\sum_{h,j\in \mathrm{G}}\left(W_{ji}W_{ih}W_{hj}\right)^{1/3}$.

Node communicability (M_i): the communicability counts (direct and indirect) paths of all lengths between two nodes and is defined by the operation: $M_{ji} = \sum_{k=0}^{\infty}\left(\frac{\boldsymbol{H}^k}{k!}\right)_{ji}$, where $\boldsymbol{H} = \mathbf{D}^{-\frac{1}{2}}\,\mathbf{W}\,\mathbf{D}^{\frac{1}{2}}$ and $\mathbf{D} \in \mathbb{R}^{N\times N}$ is the matrix with diagonal elements $D_{ii} = \sum_{j\in \mathrm{G}} \mathrm{W}_{ji}$. We use a *node communicability* instead, which is obtained from adding the communicabilities between node i and every other node in the graph. Thus:

$$M_i = \sum_{j\in \mathrm{G}} M_{ji}$$

2.1.4.2 Global measures

When a network is looked at entirely, the interest is on characterizing the processing of information along it. Measures of integration (e.g., characteristic path length, global efficiency) quantify to what extent the network can rapidly combine the information coming from separated components in it, and they are related to the notion of short paths. On the other hand, measures of segregation (e.g., network clustering coefficient) characterize the network in terms of the existence of groups of nodes, or clusters, in which information can be processed independently. Brain networks, for example, seem to be both integrated and segregated for functional processing[11].

List of global measures:

Characteristic path length (l): the average shortest path length in the network:

$$l = \frac{1}{N}\sum_{i\in \mathrm{G}} \frac{\sum_{j\in \mathrm{G}, j\neq i} l_{ji}^{\omega}}{N-1}$$

Radius (r): the minimum eccentricity:

$$r = \min_{i\in \mathrm{G}} e_i$$

Diameter (D): the maximum eccentricity:

$$D = \max_{i\in \mathrm{G}} e_i$$

Average clustering coefficient (C):

$$C = \frac{1}{N}\sum_{i\in \mathrm{G}} c_i$$

Global efficiency (E_g): the average inverse shortest path length in the network:

$$E_g = \frac{1}{N}\sum_{i\in \mathrm{G}} \frac{\sum_{j\in \mathrm{G}, j\neq i} \left(l_{ji}^{\omega}\right)^{-1}}{N-1}$$

2.2 State-dependent Riccati equation control

2.2.1 The quadratic regulator. Cost function

Control theory studies how to manipulate a system so it produces a certain desired response[17]. In optimal control, the system is steered in such a way that a defined cost function (also known as performance index) is minimized[37]. Let us assume a generic n −dimensional dynamical system with state vector $\boldsymbol{e} \in \mathbb{R}^n$. An input vector, $u(t)$**,** feeds the system. We consider $u(t) \in \mathbb{R}$, for simplicity. The evolution of $\boldsymbol{e}$ is given by:

$$\dot{\boldsymbol{e}} = \boldsymbol{f}(\boldsymbol{e}) + \boldsymbol{B}u(t); \boldsymbol{e}(0) = \boldsymbol{e}_0 \qquad (1)$$

where $\boldsymbol{B}$ is a vector whose components are only different from zero at the $i-$th entry, as the input $u(t)$ is applied over e_i.

In regulator problems, the system is required to maintain a steady state. A quadratic cost index is to be minimized in a time interval far bigger than the system's time scales (infinite time):

$$J = \frac{1}{2}\int_0^\infty [\boldsymbol{e}(t)^T \boldsymbol{Q}\boldsymbol{e}(t) + u(t)^T \boldsymbol{R}u(t)]\, dt \tag{2}$$

For J to have a minimum, it is required to be bounded from below. The weight matrices $\boldsymbol{Q}$ and $\boldsymbol{R}$ must be positive semi-definite and positive definite, respectively[17]. These matrices are chosen based on the speed of the responses and distance from the equilibrium point –the origin– that are sought to be achieved by the controller. The first term in the integral accounts for the deviations from the equilibrium whereas the second term is associated with the energy used by the controller.

2.2.2 Solution to the optimal nonlinear control problem

If the drift term, $\boldsymbol{f}$, satisfies that i) $\boldsymbol{f}(\boldsymbol{e}) \in C^m, m \geq 1$ (being C^m the set of functions with continuous derivatives up to the $m-$order) and ii) $\boldsymbol{f}(0) = 0$ (the origin is an equilibrium point), it can be rewritten as the product of the state vector and a matrix that depends on the state itself, $\boldsymbol{f}(\boldsymbol{e}) = \boldsymbol{A}(\boldsymbol{e})\boldsymbol{e}$ (apparent linearization, from now on)[37]. Under this transformation, (1) becomes:

$$\dot{\boldsymbol{e}}(t) = \boldsymbol{A}(\boldsymbol{e})\boldsymbol{e}(t) + \boldsymbol{B}u(t), \;\; \boldsymbol{e}(0) = \boldsymbol{e}_0 \tag{3}$$

In what follows, we assume that the system presents state-independent terms. In this scenario, the apparent linearization cannot be straightforwardly found[37]. However, a workaround solution[52] consists of augmenting (3) with an new equation for a stable state v, so that $\boldsymbol{e} \in \mathbb{R}^{n+1}$,

and the matrices $\boldsymbol{A}(\boldsymbol{e})$, $\boldsymbol{B}$, and the weights $\boldsymbol{Q}$ and $\boldsymbol{R}$, are extended consequently. The equation for v can be written as:

$$\dot{v}(t) = -\lambda v(t), \;\; v(0) = 1, \;\; \lambda = 1$$

If the matrix $\boldsymbol{A}(\boldsymbol{e})$ is treated as constant, the solution to (1) –with a generally nonlinear function $\boldsymbol{f}(\boldsymbol{e})$– subjected to the minimization of the cost index in (2), is found by mimicking the linear quadratic regulator formulation[36–38]. The optimal state-feedback controller is obtained in the form:

$$\boldsymbol{u}(t) = -\boldsymbol{R}^{-1}\boldsymbol{B}^{T}\boldsymbol{S}(\boldsymbol{e})\boldsymbol{e} \tag{4}$$

where $\boldsymbol{S}(\boldsymbol{e})$ is the solution to the SDRE:

$$\boldsymbol{S}(\boldsymbol{e})\boldsymbol{A}(\boldsymbol{e}) + \boldsymbol{A}^{T}(\boldsymbol{e})\boldsymbol{S}(\boldsymbol{e}) - \boldsymbol{S}(\boldsymbol{e})\boldsymbol{B}\boldsymbol{R}^{-1}\boldsymbol{B}^{T}\boldsymbol{S}(\boldsymbol{e}) + \boldsymbol{Q} = \boldsymbol{0} \tag{5}$$

2.2.3 Existence of solutions

The optimal control signal $u(t)$ exists and is obtained from solving the so-called SDRE if system (3) is observable and controllable. This means that only under certain conditions, the system can be steered to the origin at a minimum cost. Observability is guaranteed if the matrix $\boldsymbol{Q}$ is set to be positive definite. The apparent linearization yields a controllable system in a region $\mho \in \mathbb{R}^{(n+1)}$ if the matrix $\left[\boldsymbol{B}|\boldsymbol{A}(\boldsymbol{e})\boldsymbol{B}|\ldots|\boldsymbol{A}^{(n)}(\boldsymbol{e})\boldsymbol{B}\right]$ has rank $(n+1)$ for every $\boldsymbol{e} \in \mho$ (in other words, if it is pointwise controllable in the linear sense in $\mho$)[37,38]. Otherwise, the system is said to be uncontrollable and an infinite input would be required to steer the states towards the origin. Note how it is clarified inside the parenthesis that the dimension of the system is extended from n to $n+1$ to account for the possible presence of state-independent terms.

2.2.4 Numerical methods

The system (3) is iteratively solved using a Local Linearization scheme, which is known to be stable and preserves nonlinearities[20,53,54]. Given the solution at the time instant m, $\boldsymbol{e}_m$, the value of the apparent linearization, $\boldsymbol{A}_m(\boldsymbol{e}_m)$, and the solution to the SDRE, $\boldsymbol{S}_m(\boldsymbol{e}_m)$, at that same instant, the state vector at the next iteration is given by:

$$\boldsymbol{e}_{m+1} = \boldsymbol{e}_m + \boldsymbol{L}e^{\boldsymbol{C}_m\Delta t}\boldsymbol{V}$$

where $\boldsymbol{L} = \left[\boldsymbol{I}_{(n+1)\times(n+1)}, \boldsymbol{0}_{(n+1)\times 2}\right]$, $\boldsymbol{V} = \left[\boldsymbol{0}_{1\times((n+1)+1)}, 1\right]^T$ and the $\big((n+1)+2\big) \times \big((n+1)+2\big)$ matrix $\boldsymbol{C}_m$ is defined by blocks as:

$$\boldsymbol{C}_m = \begin{bmatrix} \dot{\hat{\boldsymbol{f}}}_m(\boldsymbol{e}_m) & \boldsymbol{0}_{(n+1)\times 1} & \hat{\boldsymbol{f}}_m(\boldsymbol{e}_m) \\ 0 & 0 & 1 \\ 0 & 0 & 0 \end{bmatrix}$$

in which, from (3) and (4): $\hat{\boldsymbol{f}} = [\boldsymbol{A}(\boldsymbol{e}) - \boldsymbol{B}\boldsymbol{R}^{-1}\boldsymbol{B}^T\boldsymbol{S}(\boldsymbol{e})]\boldsymbol{e}$, and $\dot{\hat{\boldsymbol{f}}}$ represents its derivative with respect to the variables, $\boldsymbol{e}$.

At each iteration, the solution to the SDRE is obtained by using MATLAB's function *lqr.m*. In practice, the controllability condition is checked while the numerical integration of the system is performed. The parametrization $\boldsymbol{f}(\boldsymbol{e}) = \boldsymbol{A}(\boldsymbol{e})\boldsymbol{e}$ conduces to locally linear systems at each time instant. Thus, the assessment of the controllability condition is also pointwise-managed through *lqr.m*, as it returns an error for uncontrollable systems.

Chapter Three: **Results**

3.1 A framework for optimal nonlinear control of brain networks

The brain behaves as a nonlinear system. Here, a framework for converting one state of brain activity into another is developed. This SDRE-based approach, not only considers the nonlinear nature of the brain, but also finds the least energy-consuming signal that can revert a pathological state. The interaction of the state variables in the dynamical model is built over connectivity matrices that are computed from real data. As such, the implementation of our framework conduces to reliable subject-specific information for controlling the activity.

3.1.1 Dynamical model

We chose a mathematical model that balances simplicity and physiological reliability. This consists of a set of Duffing-like oscillators[55], linearly coupled through either the SF and SW network models or the anatomical connection density matrices, $\boldsymbol{W} \in \mathbb{R}^{N\times N}$. Here, N is the number of nodes in the network ($N = 78$). The state variables $\boldsymbol{x}$ are interpreted as excitatory postsynaptic potentials in a neural mass formulation[54,56–58] (units: mV). Neural mass models customarily include a sigmoid activation function with lumped (average) parameters over a macroscopic population of neurons[58,59]. In the low activity limit, the sigmoid function can be replaced by a third-order approximation[60]. Then, in the model we use, the dynamics in area i is described by:

$$\begin{aligned} \dot{x}_i &= y_i \\ \dot{y}_i &= -\alpha x_i - \gamma x_i^3 + \beta \sum_{j=1}^{N} \mathrm{W}_{ji} x_j \\ \boldsymbol{x}(0) &= \boldsymbol{x}_0, \;\; \boldsymbol{y}(0) = \boldsymbol{y}_0 \end{aligned} \tag{6}$$

where $\boldsymbol{z} = [\boldsymbol{x}, \boldsymbol{y}]^T \in \mathbb{R}^n, n = 2N$ is the state vector and β is the strength of the coupling. The parameter γ is the strength of the nonlinearity. The limit case of a linear system is readily achieved

by making $\gamma = 0$. Additionally, we know that the amplitude of the solutions to system (6) grows with the initial conditions, $\boldsymbol{z}_0 = [\boldsymbol{x}_0, \boldsymbol{y}_0]^T$, and the frequency, with α, based on previous studies for the oscillations of Duffing equations with cubic nonlinearities[55].

3.1.2 Control tasks

The solution to system (6) can be tuned to reproduce different patterns of brain activity. For example, a spectrum with high power in the theta band, established globally in all the nodes, is obtained with slightly high initial conditions $\boldsymbol{z}_0 = [\boldsymbol{x}_0, \boldsymbol{y}_0]^T$ and a parameter α giving oscillations in that regime. This also stands for an alpha-band oscillation, and so on. Let us distinguish two different solutions to system (6): $\boldsymbol{z}_1$, if $\alpha = \alpha_1$, and $\boldsymbol{z}_2$, if $\alpha = \alpha_2$. The control task consists of steering the nonlinear system that results from making $\alpha = \alpha_1$ in (6) to the one obtained when $\alpha = \alpha_2$ by applying an input that enters only one node in the network. Jayaram and Tadi[38] previously introduced the idea of synchronizing two nonlinear systems by using SDRE though focused on low-dimensional generic systems and with no specific application.

Let us write $\boldsymbol{e} = \boldsymbol{z}_1 - \boldsymbol{z}_2$, as the difference between the two solutions. Now, let us look for a stimulus $u(t)$ –the controller– that optimally makes $\boldsymbol{e}$ as small as possible. Under the conditions in Section 2.2.2, the system for the difference can be written as equation (3), and SDRE control as explained in 2.2 can be applied. In this work, we choose the following apparent linearization:

$$\boldsymbol{A}(\boldsymbol{e}) = \begin{bmatrix} \mathbf{0}_{N\times N} & \boldsymbol{I}_{N\times N} & \mathbf{0}_{N\times 1} \\ \widetilde{\boldsymbol{A}} & \mathbf{0}_{N\times N} & \left\{\dfrac{-(\alpha_1-\alpha_2)\boldsymbol{x}}{v}\right\} v \\ \mathbf{0}_{1\times N} & \mathbf{0}_{1\times N} & -\lambda \end{bmatrix}$$

$$\tilde{A}_{ji} = \begin{cases} -\alpha_1 - \gamma(e_{xi}^2 + 3e_{xi}x_i + 3x_i^2) & i = j \\ \beta \mathrm{W}_{ji} & otherwise \end{cases} \tag{7}$$

where the symbol e_{xi} represents the $i-$th difference of the two solutions in the observable variables only, $e_{xi} = (\boldsymbol{x}_1 - \boldsymbol{x}_2)_i$. Note that the right-most column in matrix $\boldsymbol{A}(\boldsymbol{e})$ accounts for the state-independent terms resulting from subtracting the two solutions.

New, different systems are generated if the connectivity matrices, $\boldsymbol{W}$, are changed. Thus, the control task of converting one pattern of activity into the other is not only dependent on the dynamical model we choose for a neuronal population and its parameters, but also on the connections between the neuronal populations. For example, if these are anatomical connection density matrices, new results for the control tasks are obtained every time a new subject is considered. Additionally, by changing the position of the non-zero element in $\boldsymbol{B}$, all possible 'stimulations' to single nodes are covered. To be precise, there are as many control tasks and controllers in our model as combinations of networks and nodes receiving the control input in those networks.

To classify the efficacy of the controllers, the energy associated with the controlling signal is used. Roughly speaking, the energy is defined as the time-integral of the norm of the control input, $u(t)$ (see Section 2.2.1), and constitutes a unique performance index per network and node receiving the input.

3.1.3 Parameters and implementation

Table 3-1 summarizes the set of parameters used throughout the study. The values for the global coupling strength, β, and the initial conditions are set to produce EEG-like activity. In the same way, the 'time constants', α_1 and α_2, are chosen so that the dynamics we obtain are basically oscillations at approximately $6.4Hz$ and $8.0Hz$, respectively. These constants are within the range

corresponding to theta-alpha activity, determined by Zavaglia et al.[61]. The control tasks are assessed for strengths of the nonlinearity, γ, from 0 to 300, with incremented step size of 50.

All the simulations and analysis in this work were implemented and performed within MATLAB R2017a (The MathWorks Inc., Natick, MA, USA). The function *NLduff_ADNI_hd_subject.m* (in the Appendix to this thesis) reflects the computational procedure that was carried on for the assessments of the control tasks in Section 3.3.

Table 3-1: **Values of the parameters used.**

Parameter	Description	Value, units
α_1	'Time constant' for the $\boldsymbol{z}_1$-system	$1935\ s^{-2}$
α_2	'Time constant' for the $\boldsymbol{z}_2$-system	$2852\ s^{-2}$
β	Global coupling strength	$150\ s^{-2}$
γ	Strength of the nonlinearity	$[0{:}\,50{:}\,300]\ s^{-2}mV^{-2}$
$(\boldsymbol{x}_0, \boldsymbol{y}_0)_1$	Initial conditions for the $\boldsymbol{z}_1$-system	$[0.2 \cdot \mathbf{1}_{N\times 1}\ mV; \mathbf{0}_{N\times 1}\ s^{-1}mV]$
$(\boldsymbol{x}_0, \boldsymbol{y}_0)_2$	Initial conditions for the $\boldsymbol{z}_2$-system	$[0.1 \cdot \mathbf{1}_{N\times 1}\ mV; \mathbf{0}_{N\times 1}\ s^{-1}mV]$
$\boldsymbol{R}$	Weight for the influence the control signal has in the cost J	$1\Omega^{-1}$
$\boldsymbol{Q}$	Weight for the influence the state vector has in the cost J	$\begin{bmatrix} \boldsymbol{I}_{N\times N} & \mathbf{0}_{N\times(N+1)} \\ \mathbf{0}_{(N+1)\times N} & \mathbf{0}_{N\times(N+1)} \end{bmatrix} \Omega^{-1}$

3.2 Exploring on synthetic network models

As aforementioned, the human brain possesses scale-free and small-world properties. The study of the control tasks in SF and SW models constitutes an initial step in this work to provide: 1) evidence on the viability of the optimal nonlinear network control framework in the way it was designed, and 2) insights into the performance of the controllers in synthetic networks that are similar to the real anatomical networks. Thus, we randomly generated SF and SW binary graphs, with the same number of nodes that the anatomical networks have (78 brain regions) and with parameters that ensured their similarity to the real networks (see Sections 2.1.1 and 2.1.2).

In this exploratory analysis, we set $\boldsymbol{z}_2 = \mathbf{0}$ ($\boldsymbol{e} = \boldsymbol{z}_1$), which, in other words, means looking for optimal stimuli that send all the oscillators to the equilibrium point. The effect of a controller over the activity produced in one of the SF (SW) networks is shown in Figure 3-1a (Figure 3-1b) for illustrative purposes. It is seen how the application of the input (obtained through SDRE) is followed by a decrease on the amplitude of the oscillations until they are considerably close to the origin by the end of the simulation.

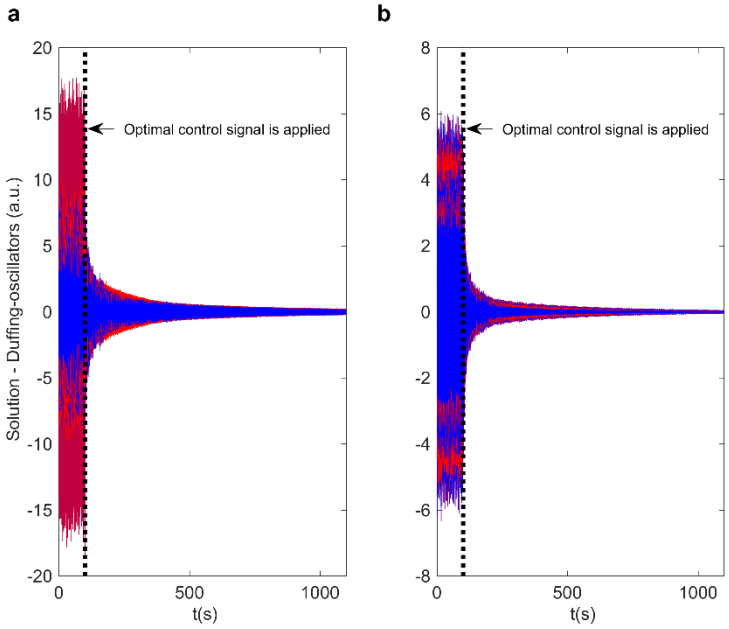

Figure 3-1: **Controlling oscillations in synthetic networks. a**) Scale-free network. **b**) Small-world network. Initially, the model produces oscillations at approximately 6.4 Hz. A controller feeds one of the nodes in the system at $t = 100s$, with the objective of making all the oscillators to evolve towards the origin. All the state variables are shown.

If the input was placed over a different node, the system might or might not be controllable. In effect, when moving the controller over all the nodes and networks, some cases of uncontrollable systems appeared. In those situations, a minimum energy signal that regulates the

system to the origin does not exist, so an infinite input signal would be required. Therefore, an uncontrollable system is associated with an infinite energetic cost of controlling (whereas the inverse of the cost will be zero). To overcome the presence of uncontrollable systems with proper visualization tools, we chose the inverse of the cost as the variable of interest for characterizing the performance of the controllers in our tasks. Thus, a node with high inverse of the cost is associated with enhanced optimal control (the full network can be readily controlled with an input entering such node).

To gain further insight into the nodes offering the best optimal control perspectives, we studied the relationship between the inverse of the costs and the local topological measures. The chosen topological measures were node degree, d_i; eccentricity, e_i; closeness centrality, q_i; betweenness centrality, b_i; clustering coefficient, c_i and communicability, M_i. In Figure 3-2a-f we show the above-mentioned dependences for 5 SF networks. Figure 3-3a-f present the same analysis for 5 different SW networks. The Pearson correlation coefficients, r, and the p-values, P, are inserted in each panel. The F-statistics for the regressions appear in the figure captions. The strength of the nonlinearity was set to $\gamma = 200\ s^{-2}mV^{-2}$ in all the simulations in this section.

These topological quantities classify the degree of 'importance' a node has in the network. For example, a low eccentricity denotes short paths from a node to the rest of the network, which is also interpreted as a high closeness centrality, whereas communicability counts direct and indirect paths of all lengths between two nodes. The strength accounts for both, the number of connections a node has and the value of the connection weights. On the other hand, high values of betweenness centrality relate to nodes that act as bridges in the network and a high clustering coefficient means tendency to form triangles, or cluster together. All the significant relationships

in Figures 3-2 and 3-3 suggest that the better-connected nodes are also the top targets for controlling the oscillatory dynamics.

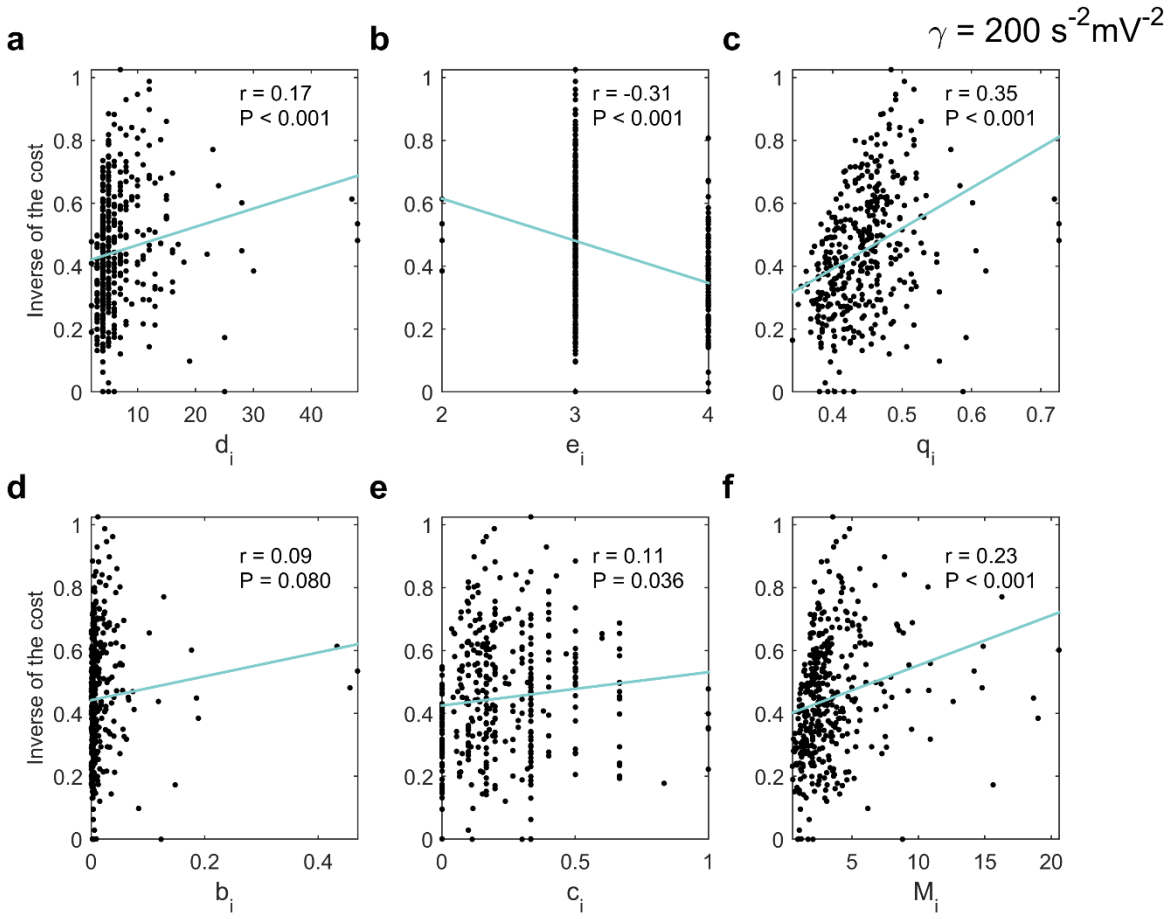

Figure 3-2: **The effect of the local topological measures in the performance of the controllers – scale-free networks.** Relationship between the inverse of the cost and the node strength (**a**) (linear regression: $F(1,388) = 11.05$, $P < 0.001$), eccentricity (**b**) (linear regression: $F(1,388) = 41.48$, $P < 0.001$), closeness centrality (**c**) (linear regression: $F(1,388) = 52.98$, $P < 0.001$), betweenness centrality (**d**) (linear regression: $F(1,388) = 3.08$, $P = 0.080$), clustering coefficient (**e**) (linear regression: $F(1,388) = 4.43$, $P = 0.036$) and communicability (**f**) (linear regression: $F(1,388) = 21.26$, $P < 0.001$); n = 390 nodes (5 networks), in all cases. The Pearson correlation coefficients, r, are inserted. The strength of the nonlinearity was set to $\gamma = 200\ s^{-2}mV^{-2}$.

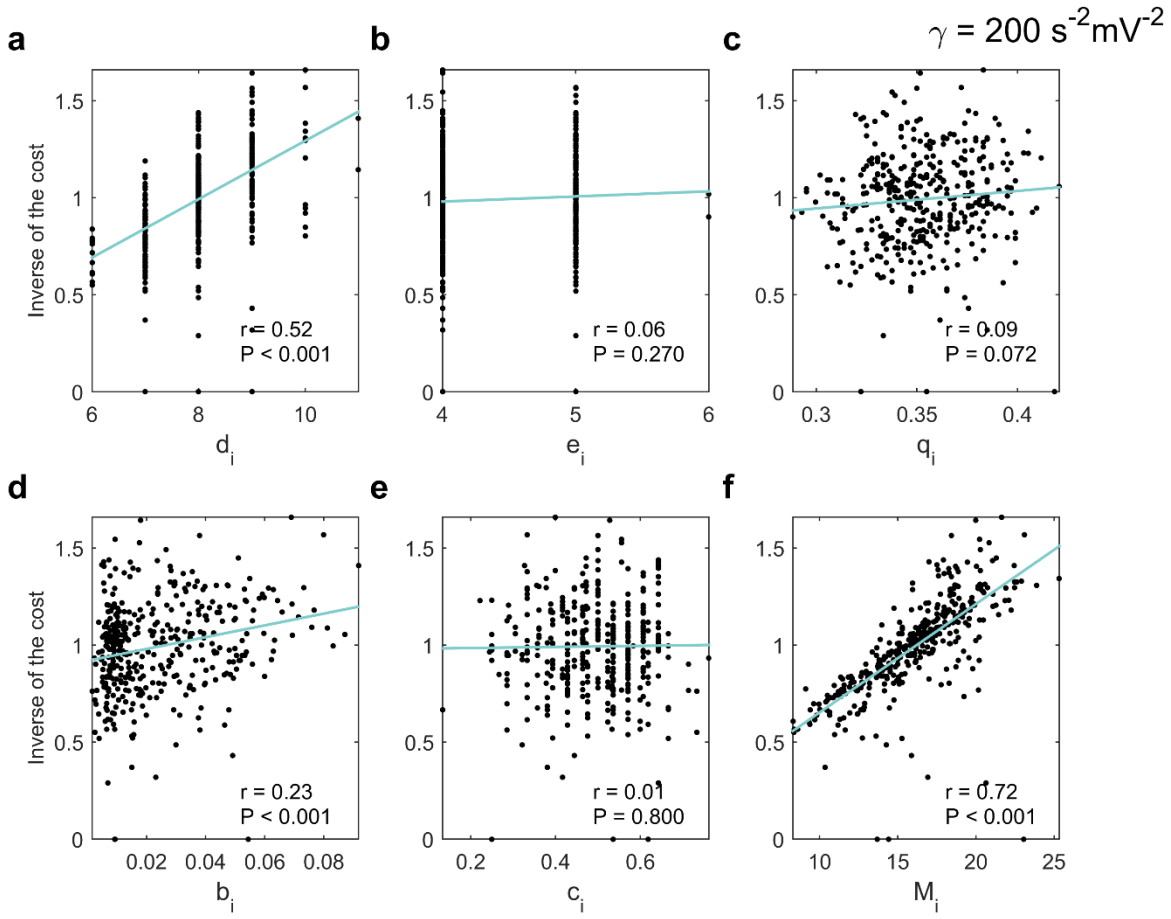

Figure 3-3: **The effect of the local topological measures in the performance of the controllers – small-world networks.** Relationship between the inverse of the cost and the node strength (**a**) (linear regression: $F(1,388) = 144.04$, $P < 0.001$), eccentricity (**b**) (linear regression: $F(1,388) = 1.19$, $P = 0.270$), closeness centrality (**c**) (linear regression: $F(1,388) = 3.26$, $P = 0.072$), betweenness centrality (**d**) (linear regression: $F(1,388) = 22.08$, $P < 0.001$), clustering coefficient (**e**) (linear regression: $F(1,388) = 0.06$, $P = 0.800$) and communicability (**f**) (linear regression: $F(1,388) = 411.60$, $P < 0.001$); n = 390 nodes (5 networks), in all cases. The Pearson correlation coefficients, r, are inserted. The strength of the nonlinearity was set to $\gamma = 200\ s^{-2}mV^{-2}$.

3.3 Controlling the Alzheimer's network

We applied the SDRE optimal control framework to each of the 41 patients from the ADNI's database, whose macroscopic electrical brain activity was given by the system of Duffing-like oscillators coupled through the anatomical connection matrices (see Section 2.1.3). A pathological state, $\boldsymbol{z}_1$, was defined as one in which all oscillators presented high-amplitude theta-band frequencies. Conversely, in a healthy state ($\boldsymbol{z}_2$), they oscillated with an alpha-band frequency. This designation of the pathological and healthy states sought to match the slowing of the EEG induced by AD[27–29]. Moreover, there is a correlation between EEG abnormalities and severity of dementia; drug-induced transient restoration of EEG normality is related to improved attention and memory performances[29,31]. Therefore, the control tasks consisted of shifting the pathological activity of the nonlinear system to healthy activity, *even though the damage the disease caused to the patient is irreversible*. In effect, the underlying pathological system –given in the model by the parameter α_1 and the affected anatomical networks, $\boldsymbol{W}$– remained unchanged. The general scheme of our methodology is presented in Figure 3-4.

3.3.1 Designing brain stimulation signals for Alzheimer's: linear vs nonlinear modeling approaches

In contrast to conventional ideas on brain stimulation where identical signals are applied regardless of subject-to-subject variability[2–6], we calculated a broad set of patient-specific signals that revert AD pathological activity, and studied their performance on the control tasks. Figure 3-5a,c,e show (respectively) the initial set-up of the temporal solutions of the nonlinear model, their behavior in the last five seconds of the simulated interval, and the optimal control signal, $u(t)$, that hypothetically enters the left pallidum, in this example, and produces a successful control task.

This corresponds to a specific subject in ADNI's database. Figure 3-5b,d,f present the same analysis for a second subject. In both cases, the strength of the nonlinearity was $\gamma = 200\ s^{-2}mV^{-2}$. This is a typical value among the strengths of the nonlinearity we tested.

As seen from the temporal evolution of variable x, which represents the postsynaptic potential over one randomly chosen region in the model, the controlled trajectory almost identically matches the desired trajectory (low-amplitude alpha oscillation) by the end of the simulation (Figure 3-5c,d). Please, note the subtle differences in the signals the controller is set to deliver from one subject (Figure 3-5e) to the other (Figure 3-5f).

These dissimilarities are mostly due to the generation of subject-dependent minimal-energy signals. The magnitudes of the calculated optimal signals (-0.1–0.1 V, approximately) were around one order lower than the signals that are currently used in deep brain stimulation for AD (3.0–3.5 V)[2,3]. The magnitude generally decreased with time although the signals possessed complicated shapes. The energetic cost of controlling the full network of oscillators was also computed. We found that low magnitude signals are associated with reduced costs (Figure 3-5e,f).

Several subject-dependent cases in which the optimal control framework failed to produce stimulation signals were obtained for nonlinear systems (see Figure 3-11). Figure 3-6 shows equivalent results to those in Figure 3-5, although obtained over linear systems ($\gamma = 0\ s^{-2}mV^{-2}$). No case of uncontrollable systems for any subject was found for signals entering the linear variant of the model though, which seems unrealistic to occur in any practical implementation. Additionally, the magnitude of the control signals obtained was generally lower for linear than for nonlinear systems. Manifestly, these results depend on the anatomical connection matrices and the dynamical model (coupled Duffing-like oscillators) we have used for the simulations.

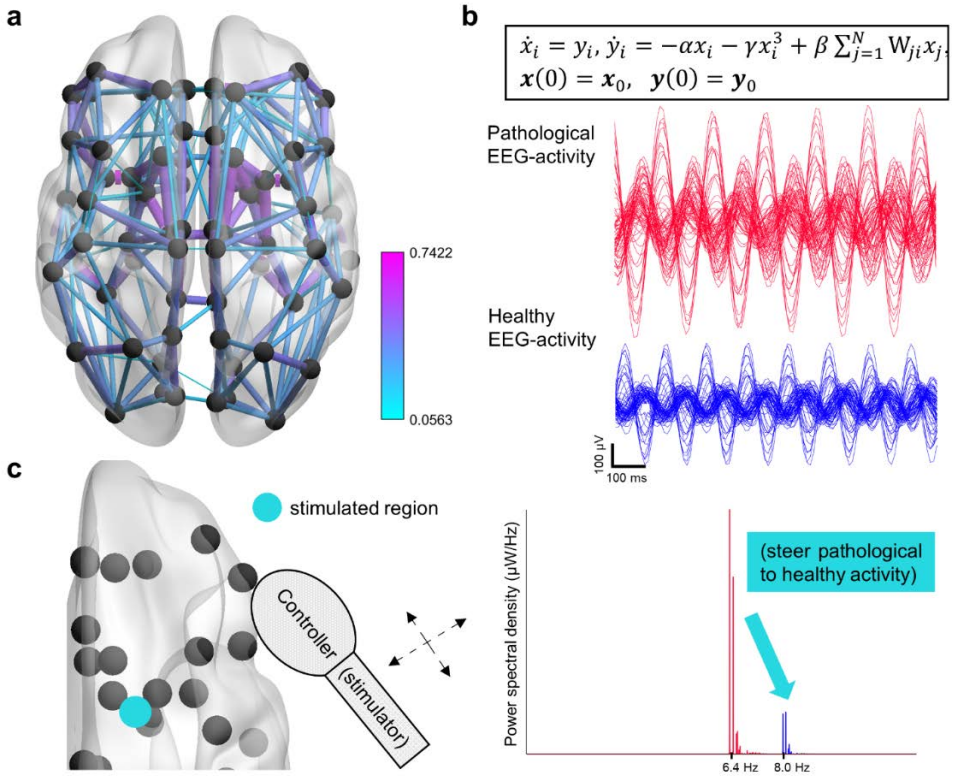

Figure 3-4: **Optimal nonlinear network control of Alzheimer's. a**) Anatomical connection density matrices ($\boldsymbol{W}$) for the interaction of 78 predefined brain regions were obtained for each of the patients in the study. The color code and size of the edges represent the weight of the connections. **b**) Duffing-like oscillators describe the activity in each brain region i, and are coupled through $\boldsymbol{W}$. The parameter γ characterizes the nonlinearity of the system. By tuning α and the initial conditions, $\boldsymbol{z_0} = [\boldsymbol{x_0}, \boldsymbol{y_0}]^T$, 'pathological EEG activity' (high-amplitude theta-band oscillations, $f \approx 6.4\ Hz$) and 'healthy EEG activity' (low-amplitude alpha-band oscillations, $f \approx 8.0\ Hz$) are obtained. **c**) A hypothetical 'controller' is moved over all the regions. The controller applies the optimal (least energy-consuming) signal that steers the activity to the healthy state, and guarantees the shift of the EEG spectrum towards higher frequencies. Each stimulus depends on the region and patient receiving it through the dynamical system that is solved.

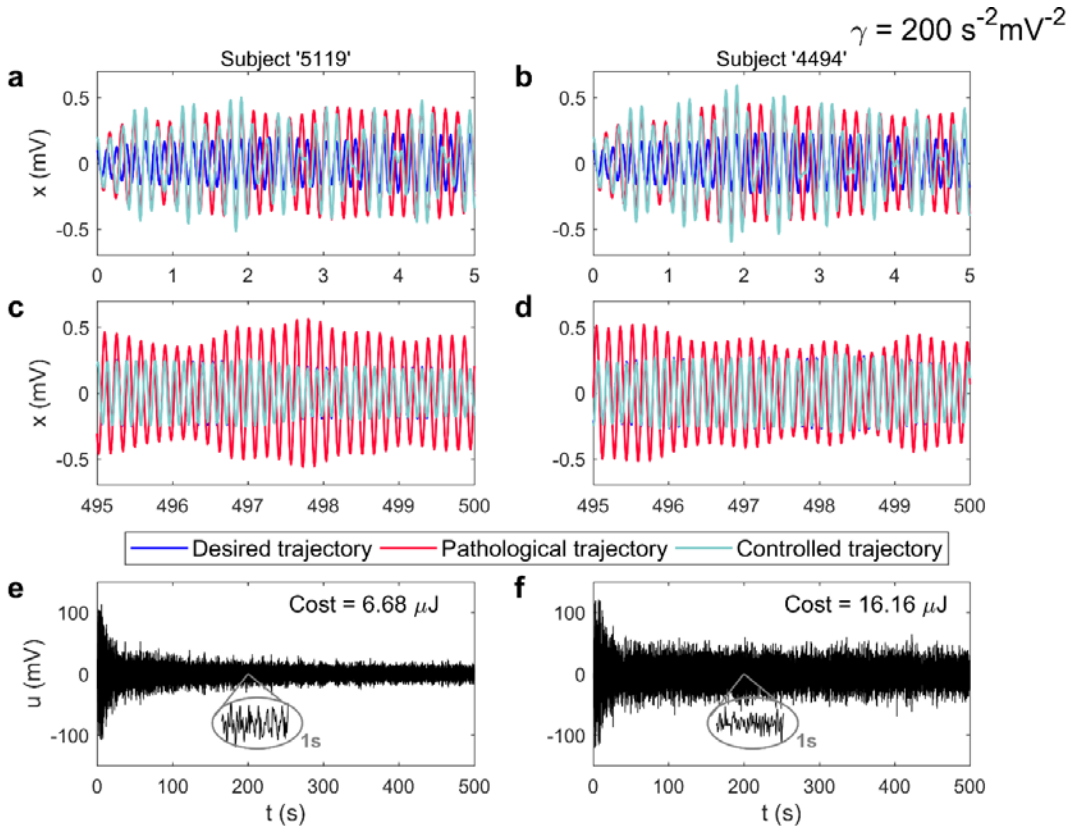

Figure 3-5: **Controlling the Alzheimer's pathological EEG activity (nonlinear case). a**) Start of the simulations for the ADNI subject identified as '5119'. The evolution of the postsynaptic potential over one region is shown only. Others behave analogously. The desired trajectory corresponds to a 'healthy' low-amplitude alpha-band oscillation. The model can also produce 'pathological' high-amplitude theta-band oscillations. A control signal feeds the left pallidum for reverting the pathological activity. **c**) By the end of the simulation, the controlled trajectory almost identically matches the healthy state although it was created with the 'pathological parameters'. This is the effect of the optimal control signal, shown in (**e**). Panels (**b**,**d**,**f**) present the same analysis for the subject identified as '4494'. The energetic cost of the control task is inserted in **e** and **f**. A one-second zoom-in window of the control signal at $t = 200s$ is also inserted. The strength of the nonlinearity was set to $\gamma = 200\ s^{-2}mV^{-2}$.

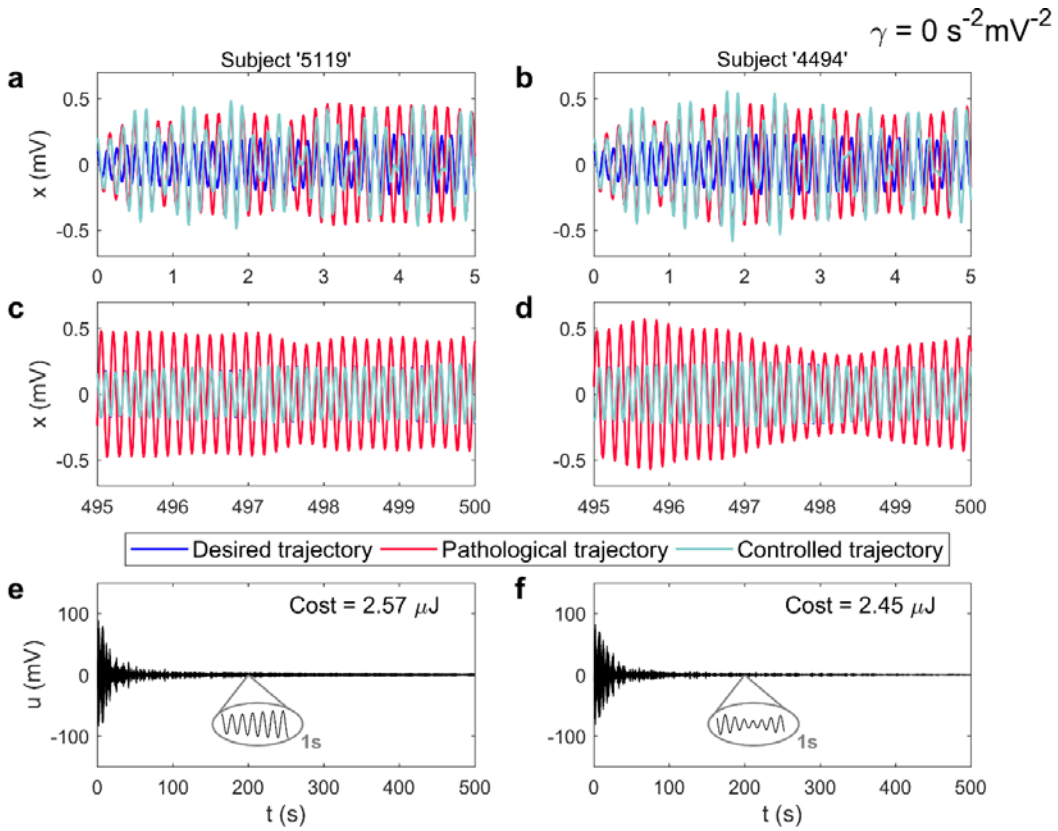

Figure 3-6: **Controlling the Alzheimer's pathological EEG activity (linear case). a**) Start of the simulations for the ADNI subject identified as '5119'. The evolution of the postsynaptic potential over one region is shown only. Others behave analogously. The desired trajectory corresponds to a 'healthy' low-amplitude alpha-band oscillation. The model can also produce 'pathological' high-amplitude theta-band oscillations. A control signal feeds the left pallidum for reverting the pathological activity. **c**) By the end of the simulation, the controlled trajectory almost identically matches the healthy state although it was created with the 'pathological parameters'. This is the effect of the optimal control signal, shown in (**e**). Panels (**b**,**d**,**f**) present the same analysis for the subject identified as '4494'. The energetic cost of the control task is inserted in **e** and **f**. A one-second zoom-in window of the control signal at $t = 200s$ is also inserted. The strength of the nonlinearity was set to $\gamma = 0\ s^{-2}mV^{-2}$.

3.3.2 Selecting the target location for stimulation: ranking the areas based on the cost of controlling the brain network

We collected the results of all simulations to construct a general picture of the power regions (nodes in the networks) have to control the AD system. Results for the simulations using the same strength of the nonlinearity, γ, were averaged across all the subjects in the study. Again, it is the inverse of the cost the variable we used for quantifying how well regions can propagate a stimulus, serving to construct a ranking.

Figure 3-7a shows the brain areas' ranking for the limit case of a linear system (mean inverse of the cost ± standard error of the mean). Top-ranked areas appear in the leftmost part of the panel. Figure 3-7b contains a graphical visualization of the brain sites where they are approximately located. The size of the spheres is directly proportional to the inverse of the cost. We found that several of the top-ranked regions are spatially close, with predominance over the left hemisphere. New rankings were obtained when the nonlinearities increased (see Figure 3-7c,d). As the magnitudes of the costs generally grow with the strength of the nonlinearity, the upper limit of the vertical axis in Figure 3-7c, representing the maximum mean inverse of the cost registered for $\gamma = 200\ s^{-2}mV^{-2}$, is smaller than the corresponding one in Figure 3-7a.

Additionally, we assessed the relationship between the rankings of the regions resulting from controlling systems with different nonlinearities. The statistical dependence between the rankings associated to the nonlinearities was measured in terms of Spearman correlation (Pearson correlation between the rankings). The Spearman's rank correlation coefficient (Spearman's rho) between the linear system's order and the corresponding to a nonlinear system with $\gamma = 100\ s^{-2}mV^{-2}$ was $\rho = 0.98\ (p < 0.001)$. It decreased to $\rho = 0.87\ (p < 0.001)$ when the

nonlinearity was increased to $\gamma = 200\ s^{-2}mV^{-2}$ and further down to $\rho = 0.59$ ($p < 0.001$) for $\gamma = 300\ s^{-2}mV^{-2}$. The orders corresponding to two consecutive nonlinearities also differed more (Figure 3-8a).

These 'expected' rankings, obtained from looking at the average inverse of the cost only, had similarities in their top and bottom-most components (Figure 3-8b), suggesting a global privileged/disadvantageous position of some areas in the brain network (see Section 3.3.3) that transcends the effects of the nonlinearities. We consider it important to note that individual cases of uncontrollable systems were ubiquitously reported when nonlinearities were considered. Only the individual calculation of the minimal-energy control signals, instead of an analysis over the main values as performed in this section, can conduce to a trustable selection of stimulation targets.

Nevertheless, it is interesting to note how regions on the top of the mean control orders (Figure 3-7a,c) belonged to a clearly defined group with prevalence in the left hemisphere: the left pallidum, left putamen, left amygdala, left hippocampus, right thalamus proper, left insula, left basal forebrain, left fusiform and the caudate nuclei. Overall, these high-ranking regions belong to the limbic system and the basal ganglia. On the other hand, the worst-ranked areas included the right postcentral gyrus, both paracentral lobule, right inferior and superior parietal lobules, left cuneus and the right temporal lobe, which can all be classified as temporoparietal regions. Temporal and parietal cortical areas are affected in AD early in the disease course[2].

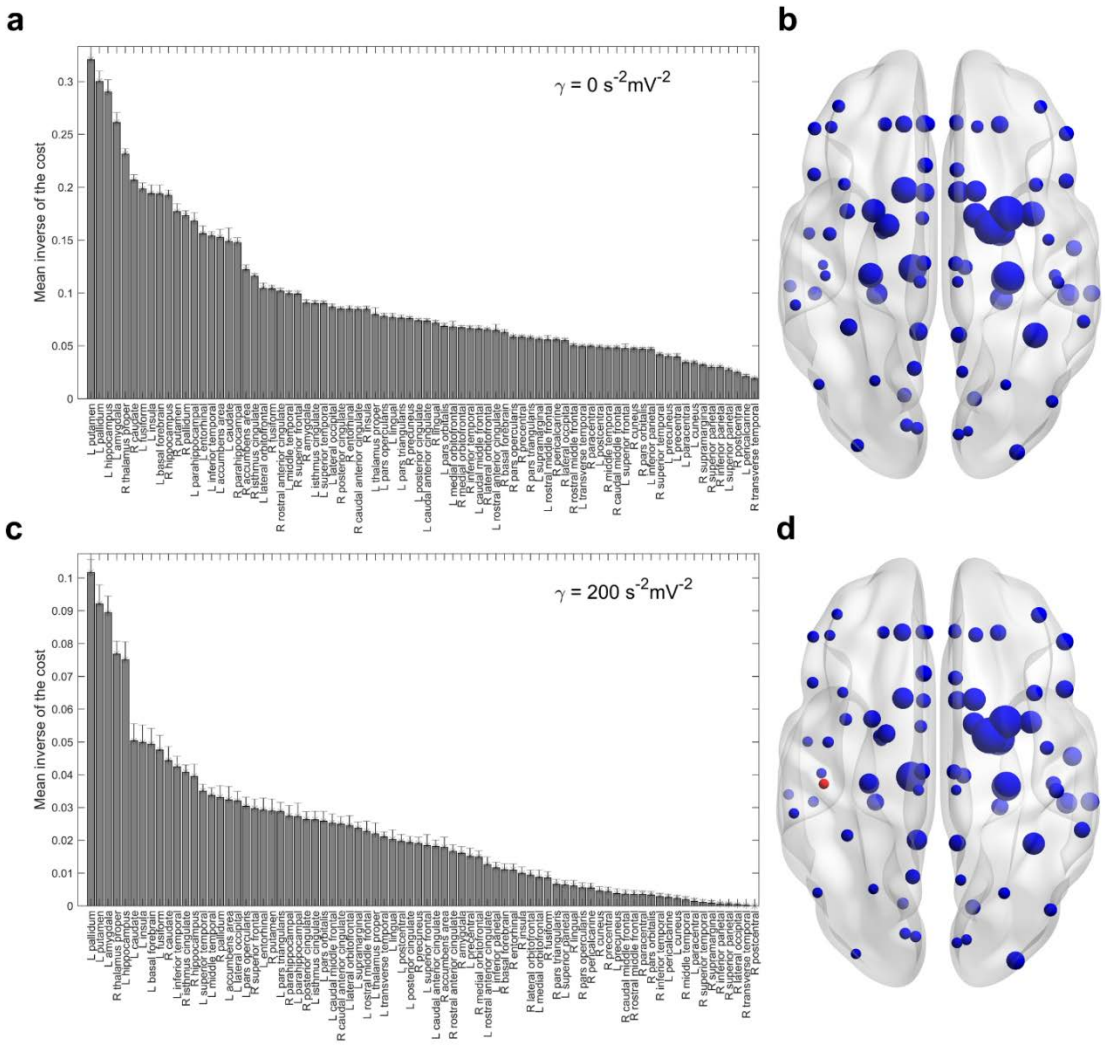

Figure 3-7: **Ranking brain regions according to the mean inverse of the cost of controlling the network. a**) Order corresponding to the linear case. Given is the mean ± s.e.m. of n = 41 subjects. Inputs entering regions in the leftmost part of the order control Alzheimer's activity at a lowest cost. **b**) Graphical representation with the approximated location of the brain regions. The size of the spheres is directly proportional to the mean values in panel **a**. Panels (**c**,**d**) are analogous to (**a**,**b**) except that the strength of the nonlinearity has been set to $\gamma = 200\ s^{-2}mV^{-2}$ and a new ranking is obtained. The red sphere represents the right postcentral gyrus, which yielded uncontrollable nonlinear systems for all the subjects in the sample.

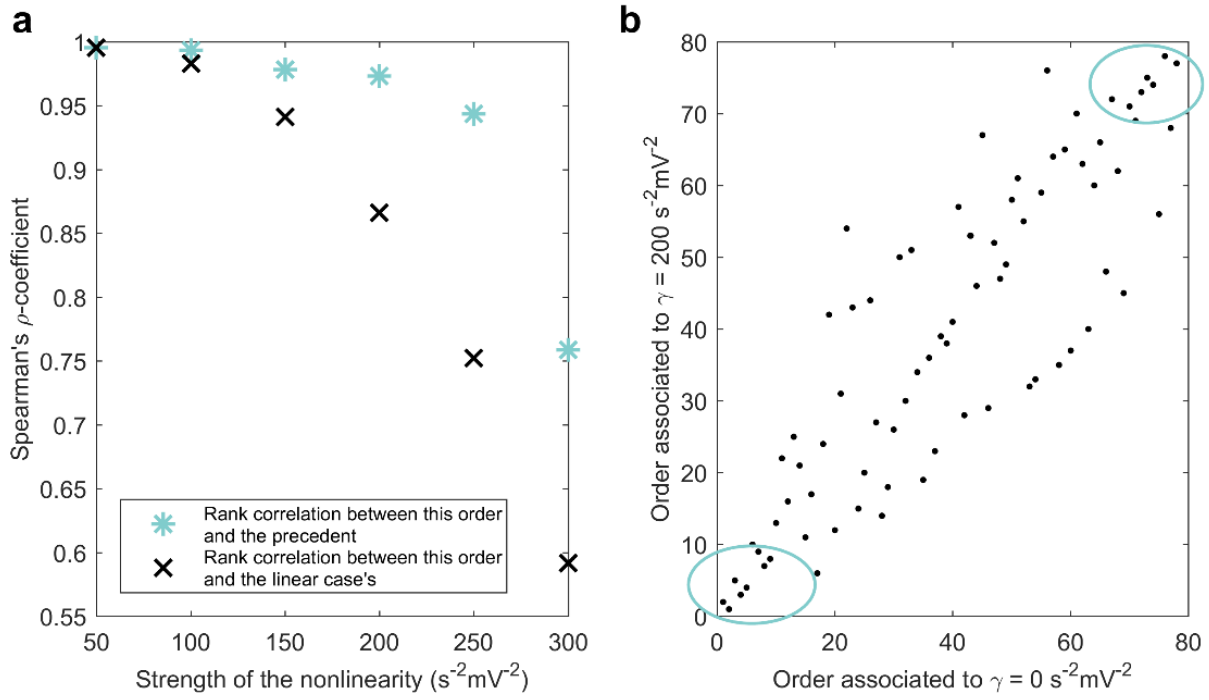

Figure 3-8: **Nonlinearity-related changes to the average brain regions' ranking. a**) Rank correlations between the orders corresponding to different nonlinearities (paired t-test: large-sample approximation, P < 0.001 in all the cases, n = 78 regions). As the nonlinearity increases, the Spearman's rho coefficients for the correlation between a ranking and both, the order corresponding to the previous nonlinearity and to the linear case, decrease. **b**) The rankings for the nonlinearities $\gamma = 0\ s^{-2}mV^{-2}$ and $\gamma = 200\ s^{-2}mV^{-2}$ are compared. These orders are similar in their top and bottom-most parts (inserted ellipses) and dissimilar in between.

3.3.3 Network topology helps to select stimulation candidates

Identifying the most suitable candidates for a successful brain stimulation treatment remains a challenge. Even subjects suffering from the same condition are intrinsically different due to

genetic and environmental factors[62]. Here, we aimed to create a gold standard for selecting both stimulation sites and individuals most likely to benefit from stimulation therapy based on the subject's anatomical networks estimated from DW-MRI data. We looked at the relationship between the results of the control tasks and the topological characteristics of the networks, $\boldsymbol{W's}$, over which they are performed.

Figure 3-9 is analogous to Figures 3-2 and 3-3, except that it is the mean inverse of the cost that is shown. We found significant correlations between the mean inverse of the cost of controlling the brain network from a region and all the local measures (s_i, e_i, q_i, b_i, c_i and M_i). The only decreasing relationship found was with the eccentricity, e_i, meaning that regions with a small shortest path length might constitute the more suitable targets for controlling the network. On the other hand, nodes with high s_i, q_i, b_i, c_i and M_i were associated with high mean inverse of the cost. Analyzing the strength of the correlations revealed an interesting pattern: the three correlation coefficients appearing on the top row of Figure 3-9 –for quantities strictly related to direct connections– were considerably higher than those on the bottom which relate to measures for quantifying relay nodes, segregation levels and indirect paths, respectively. This suggests that direct links (high weights, small shortest paths) between nodes are what makes a stimulus fully propagate over a network to reach the control objective at a low energetic cost.

What is presented in Figure 3-9 stands for all the strengths of the nonlinearity we tested. However, the magnitudes of the correlation coefficients were higher as the strength of the nonlinearity decreased. The same analysis presented in Figure 3-9 can be found in Figure 3-10 for the linear systems.

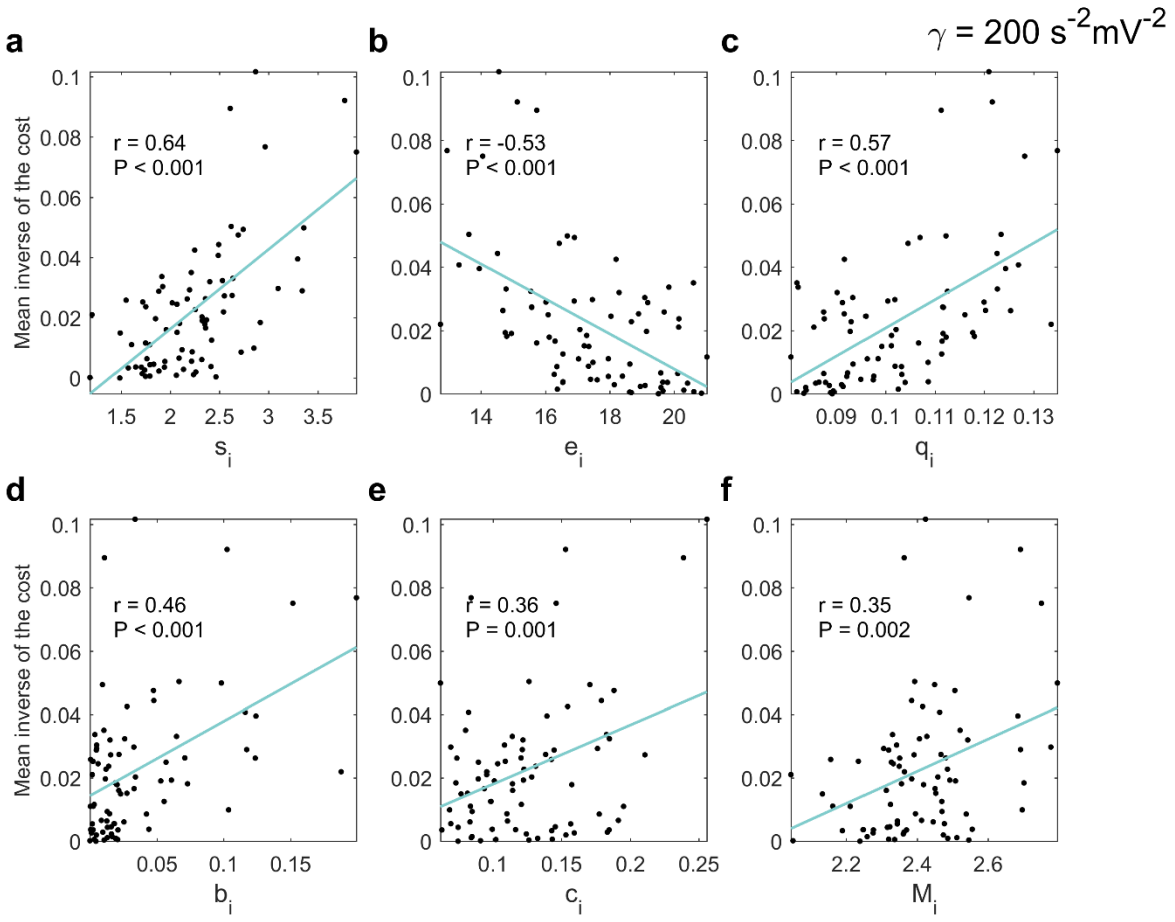

Figure 3-9: **The effect of the local topological measures in the performance of the controllers – Alzheimer's anatomical networks (nonlinear case).** Relationship between the mean inverse of the cost across the sample and the mean node strength (**a**) (linear regression: $F(1,76) = 55.95$, $P < 0.001$), eccentricity (**b**) (linear regression: $F(1,76) = 29.61$, $P < 0.001$), closeness centrality (**c**) (linear regression: $F(1,76) = 36.94$, $P < 0.001$), betweenness centrality (**d**) (linear regression: $F(1,76) = 20.90$, $P < 0.001$), clustering coefficient (**e**) (linear regression: $F(1,76) = 11.36$, $P = 0.001$) and communicability (**f**) (linear regression: $F(1,76) = 10.87$, $P = 0.002$); n = 78 regions, in all cases. The Pearson correlation coefficients, r, are inserted. The strength of the nonlinearity was set to $\gamma = 200\ s^{-2}mV^{-2}$.

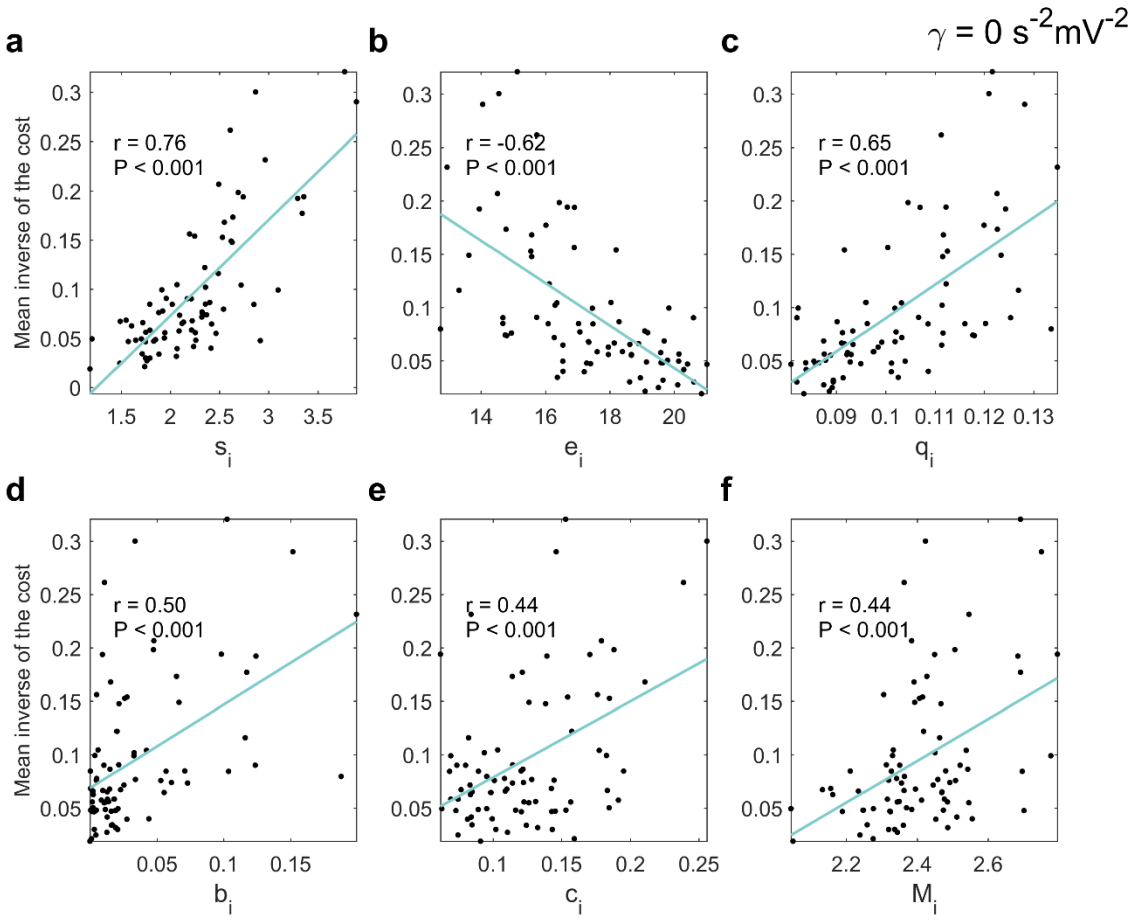

Figure 3-10: **The effect of the local topological measures in the performance of the controllers – Alzheimer's anatomical networks (linear case).** Relationship between the mean inverse of the cost across the sample and the mean node strength (**a**) (linear regression: $F(1,76) = 105.72$, $P < 0.001$), eccentricity (**b**) (linear regression: $F(1,76) = 46.58$, $P < 0.001$), closeness centrality (**c**) (linear regression: $F(1,76) = 55.70$, $P < 0.001$), betweenness centrality (**d**) (linear regression: $F(1,76) = 25.20$, $P < 0.001$), clustering coefficient (**e**) (linear regression: $F(1,76) = 18.70$, $P < 0.001$) and communicability (**f**) (linear regression: $F(1,76) = 18.26$, $P < 0.001$); n = 78 regions, in all cases. The Pearson correlation coefficients, r, are inserted. The strength of the nonlinearity was set to $\gamma = 0\ s^{-2}mV^{-2}$.

As previously expressed, a set of inputs entering certain specific regions for each subject failed to convert theta activity into alpha activity. The number of successful signals thus provides a good estimate of how responsive the patients would be to the tentative treatment herein modeled. Therefore, we studied the relationship between the number of inputs resulting in controlling the systems and global measures of the subjects' anatomical network. This is shown in Figure 3-11a-d (characteristic path length, l; radius, r; average clustering coefficient, C, and global efficiency, E_g, in this order). We found that subjects with small average shortest path length (l) of their anatomical networks were controlled by more inputs –in other words, from a high number of regions. In the same way, the lower the radius was, the more inputs were efficient in the control tasks. More clustered networks yielded the same result. Finally, the number of areas from which the AD brain can be controlled per subject was also proportionally related to the global efficiency, a measure that reflects how efficiently information can be exchanged over the network. We did not obtain any significant correlation between the number of controllable dynamical systems and the diameter of the networks. There are no linear systems-equivalent results to the ones in Figure 3-11 as all the stimuli yielded controllable systems in that case.

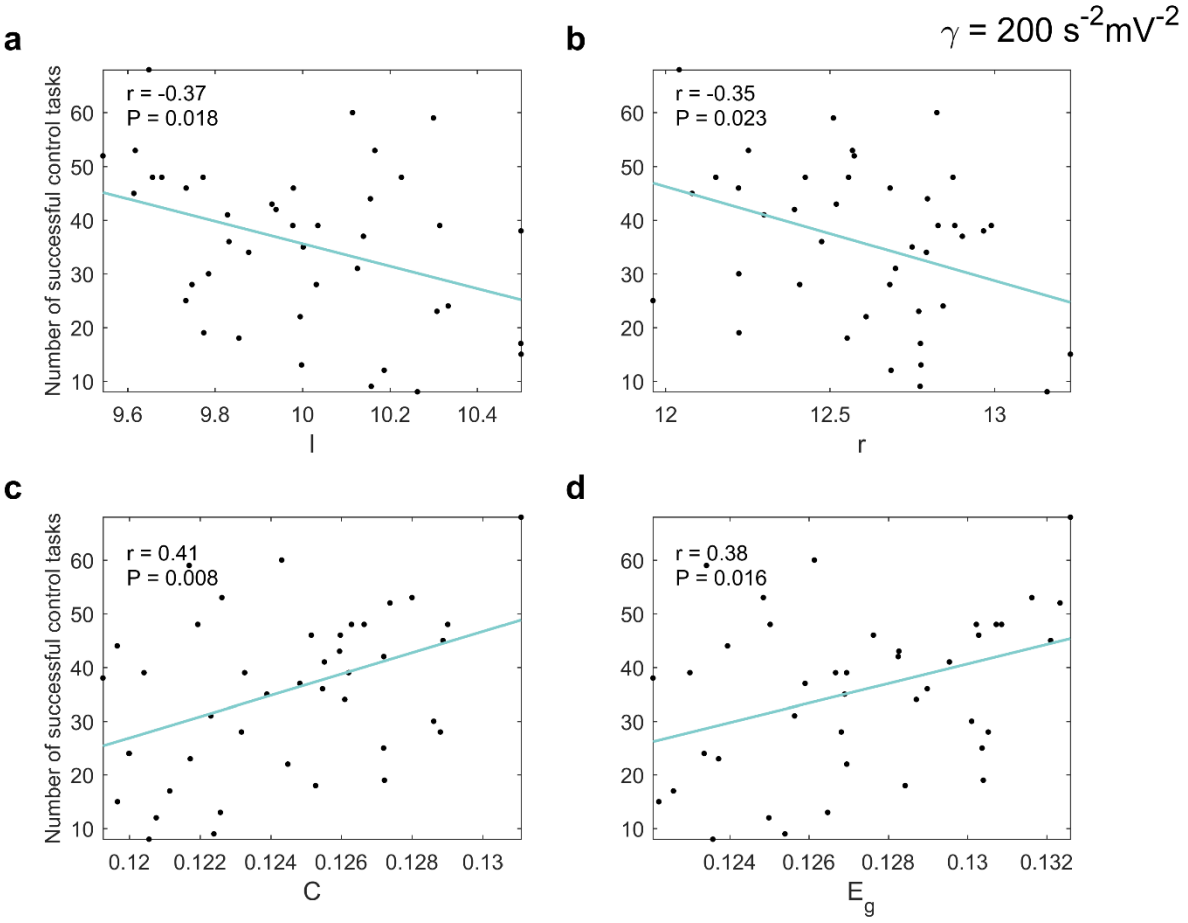

Figure 3-11: **The effect of the global topological measures in the success of the control tasks.** Relationship between the number of successful control tasks per subject –the maximum possible value being 78– and the characteristic path length (**a**) (linear regression: F(1,39) = 6.08, P = 0.018), radius (**b**) (linear regression: F(1,39) = 5.60, P = 0.023), average clustering coefficient (**c**) (linear regression: F(1,39) = 7.77, P = 0.008), and global efficiency (**d**) (linear regression: F(1,39) = 6.39, P = 0.016); n = 41 subjects, in all cases. The Pearson correlation coefficients, r, are inserted. The strength of the nonlinearity was set to $\gamma = 200\ s^{-2}mV^{-2}$.

Chapter Four: **Discussion**

In this thesis, we introduced a framework for calculating the optimal signals and most suitable regional targets in the brain for controlling AD activity, catered to individual subjects. Unlike other studies[1,7–9], ours considers the existence of nonlinearities in the modeling of brain dynamics by extending the use of the so-called state-dependent Riccati equation control to biological, high-dimensional systems. The calculation of the optimal signals that can propagate over the network and set its temporal dynamics to a desired state also provides insights into the way neural systems control themselves. If a network node associates with low cost for exogenously controlling the neural system, then that same element must have certain advantaged position for the self-regulation processes occurring there.

4.1 Significance: beyond Alzheimer's disease

The goal of brain stimulation is to exogenously control (i.e., manipulate) the brain's activity so that it follows a desired pattern associated with a healthy state[63]. The specific characteristics of the signals in brain stimulation experiments/therapies are usually overlooked. Square pulses are translated from the treatment of one condition to the other (e.g., from Parkinson's to Alzheimier's[2,3]), sometimes tuned in an exploratory way, and applied identically to every subject without considering individual differences. In a world where medicine is constantly becoming more personalized, treatments which are designed using broad statistical measures and account poorly for interpatient variability are inefficient[62]. Current approaches to modeling brain stimulation present major shortcomings (see the recent review by Bassett et al.[10]) and importantly, nonlinearities are known to characterize the brain's dynamical behavior and should not be

excluded from any realistic modeling[20]. Our framework deals with all the above-mentioned limitations.

Although focused on AD in this study, our methodology is not restricted to it. Any other clinical condition characterized by abnormalities in brain dynamics (and with existing meaningful neuroimaging data for using in the modeling process) could be addressed similarly with the following scheme:

1) a model for the dynamics is assumed,

2) the model is set to produce pathological and healthy activity,

3) brain stimulation signals that revert pathological activity at the lowest possible energetic cost are found through SDRE.

4.2 Analysis on synthetic network models as the initial step

Given the novelty of the herein proposed framework, our first approach was to perform dummy control tasks over simulated connectivity networks. The SF and SW networks were chosen as binary to further simplify the calculations and avoid assigning connection weights without anatomical or physiological foundation. Therefore, the distribution of local topological measures over the 78 nodes (and 5 networks), achieved a few values in a small range. This conduced to relatively small correlation coefficients when the relationship between the topological measures and the inverse of the cost of controlling the entire network of oscillators from each of the nodes was studied. Similarly, the number of uncontrollable systems obtained as the input entered the nodes in these networks with almost identical values of the global measures, was not sufficient to construct a picture of the dependence of the success of the control tasks on the global characteristics of the SF and SW networks. However, the observed trends in the identification of

the target regions suggested that better-connected areas were also the best candidates for receiving controlling inputs. Finally, steering the electrical activity of a neural system to the origin was chosen as a test method only, and not as a real brain stimulation objective. Consequently, we did not perform any further analysis on the implications these results had for brain stimulation, which was carried on for AD afterwards.

4.3 Characteristics of the signals obtained for Alzheimer's. Effects of network topology and the nonlinear modeling

We modeled a stimulation-therapy for AD based on the correction of the EEG spectrum towards higher frequencies. As such, we looked for inputs (control signals) to individual areas of the brain that revert pathological activity at the lowest possible energetic cost. Among all the possible signals that were obtained for each subject, the one producing the fastest, least energy-consuming response, can be administered in a brain stimulation procedure. The controllers we designed have lower magnitude than what has been identified as the safety threshold[2,3] in deep brain stimulation for AD (3.0–3.5 V) and are still successful in the reversion of pathological activity.

We also studied the dependence of the optimal control tasks on the anatomical networks conditioning the dynamics. In essence, we found a strong relationship between the success of the control tasks and the topological features of the anatomical connection density matrices that served as scaffold for the interaction of the cortical and subcortical 'pyramidal neuron' populations in the model. Overall, the significant correlations existing between the mean inverse of the cost and the local topological measures suggest that nodes with high connectivity associate with low cost of controlling the full network of oscillators. Our results agree with previous findings that stimulation

to strongly connected nodes in brain networks produces low-energy transitions[1,9]. For each subject, we found that the better connected a network is –namely, a network having low average shortest path length, high clustering coefficient and/or high global efficiency–, the more inputs to individual nodes success on the control task and make the system evolve to the predetermined healthy state. Small average distance between the nodes in the network and high clustering coefficient are attributes associated to the small-worldness property[34], a concept that relates the fast spread of stimuli to the existence of 'shortcuts' in a network. The concept of small-worldness is represented in terms of efficiency on the information flow as well[64]. In short, subjects having 'a better-connected network' are seemingly the optimal candidates for AD's effects-reverting protocols. However, these indications relating optimal nonlinear control and network measures are only an approximation (based on average values), and we recommend the calculation of the optimal signals and targets for each subject to undergo our proposed brain stimulation for AD.

The inclusion of nonlinearities in our model causes several control tasks to fail for a subject, a fact that, to the best of our knowledge, has not been reported for linear brain dynamics. However, we do not expect that inputs to every neuronal conglomerate in real stimulation experiments are able to steer the (AD) brain to the desired state, given its complexity and nonlinear character[20–22]. The order in which areas were ranked according to the energy used for controlling the network, changed with the strength of the nonlinearity. Interestingly, as the strength of the nonlinearity (γ) increased, the linear dependence of the expected cost of controlling from a region on its topological characteristics was less obvious (see Figure 3-9 and Figure 3-10) –the higher the γ is, the less the systems look like sets of linear (harmonic) oscillators coupled through the anatomical connection density matrices. This likely denotes competition between the effects of the nonlinearity and the

structure of the network for the dynamical interaction, and warrants further investigation. Overall, our findings reveal the importance of using nonlinear realistic modeling to better understand brain stimulation and its accurate design.

4.4 The Alzheimer's brain influences the results

When ranking the regions in the brain according to the average cost of controlling the network with a single stimulus, we found that the lowest energetic cost was associated with limbic and basal ganglia areas, or strongly connected to them, such as the thalamus. The role of these areas in motor control, learning, memory and relay of information[65,66] engages them in a wide number of connections, and consequently (see Figure 3-9), makes them highly desirable targets for stimulation. The globus pallidi send basal ganglia information to the thalamus which projects back to the cortex[66]. Specifically, the left pallidum –at the top of the nonlinear systems ranking– has been previously identified as having the least overall multifactorial damage by AD[26]. The caudate nuclei and putamen receive and process cortical and thalamic information which is later transmitted to the globus pallidi[66]. On the other hand, the large-scale brain network topology seems to be organized to concentrate information flow in the hippocampal formation[67], structure with a key role in memory processesing[68], and also among those associated to better optimal nonlinear network control in this work. Finally, the amygdala has a broad pattern of anatomical connections, especially with other subcortical structures[69], making it another of the top targets for achieving successful control tasks.

The bulk of the poorly-ranked areas comprised temporal and parietal association cortices and sensory and motor cortices structures. Interestingly, most of these bottom-ranking areas are in the right hemisphere. Some experimental evidence supports this finding, such as reports of

increased vascular and AD burden (amyloid-β and tau deposition) in the right hemisphere, compared to the left[70]. Additionally, in one of the studies that inspired this work[2], no downstream evoked response in the right hemisphere was recorded for one patient out of six. They performed DBS of the fornix, an axonal bundle that acts as a major output and input tract for the hippocampus and the temporal lobe. The absence of a right-sided response in some subjects while indirectly stimulating several regions simultaneously, along with the recorded worsening of AD in the right hemisphere may explain the low performance of right hemisphere controllers in our work.

4.5 Towards implementation

Most top-ranked regions were subcortical structures (e.g., pallidum, amygdala, thalamus proper, hippocampus). However, other similarly-ranked areas, such as the insula, are cortical. Current brain stimulation techniques differ in reach, design and degree of invasiveness. In therapeutic practice, either one (subcortical structures) or the other (cortical structures) are targeted[4–6]. In a recent work, non-invasive deep brain stimulation of the hippocampus in living mice was achieved by Grossman et al. while applying alternating high frequency currents at slightly different frequencies over the scalp[71]. The envelope resulting from the superposition of those two fields was set to reach maximum amplitude at a site deep in the brain, consequently driving deep-lying neurons only. They were also able to produce different motor responses by changing the set of currents delivered to the mice brain. Although the pattern of currents used by Grossman et al. (sinusoidal-like) is simpler than the ones we have obtained (Figure 3-5), their work shows the possibility of stimulating neuronal sets at any depth by using superficial devices. As such, the most suitable regional target for each patient (either subcortical or cortical) could be reached by using a single device. In a previous study, Terney et al. introduced current stimulation

by high-frequency noisy signals[72] with positive results, including enhanced corticospinal excitability. The temporal profiles of the signals administered in that study somehow resembles the ones we obtained, although theirs have higher frequency, amplitude and seemingly noisier components. Together, these works indicate the feasibility of our proposal in terms of designing a device that delivers tailored signals to any location in the brain. We predict an eventual merging of our theoretical approach with cutting-edge stimulation technology like the ones proposed in the referred studies.

Another issue regarding the future development of optimal nonlinear network control of AD is the possibility of the spilling of stimulation to adjacent nuclei[73,74] as we propose to target single localized regions. Nonetheless, the lack of focality of brain stimulation techniques might be an advantage for their clinical application[74]. Several of the regions from which the desired trajectory was achieved at low energetic cost in our model have physical proximity (see Figure 3-7b,d), and could be reached in a target-specific experiment[73]. We hypothesize that simultaneous stimulation of different structures would produce faster optimal control of the pathological activity.

On the other hand, the recently-introduced adaptive deep brain stimulation (aDBS) is gaining support for replacing the conventional constant-parameters brain stimulation in the treatment of Parkinson's[75–78]. aDBS uses the subthalamic local field potential (LFP) activity recorded directly from the DBS electrode itself as a feedback for tuning the stimulation signal in real time. The level of beta frequency band oscillations in the LFP correlates with motor impairment, in the presence or absence of therapeutic interventions[75]. A brain–computer interface system uses this biomarker to control when the stimulation is applied. Thus, aDBS is a closed-loop technology[77]. Such procedure delivers less energy to the patient (with fewer side effects) and is clinically superior to

standard continuous DBS, according to the results reported in several studies[75,76]. Our framework, designed without knowledge of the existence of aDBS, aims to obtain stimulation protocols that are also assembled over the analysis of a feedback signal related to the patient's clinical condition (see equation (4)). The successful application of aDBS constitutes evidence on the favorable energetic effects of the stimulation signals for AD obtained through our approach and starts to pave the way towards its experimental validation.

4.6 Limitations

Finally, we would like to point out the pioneering nature of our work and list its methodological limitations in what follows. Further work is to be done in solving those before proceeding to demonstrate the efficacy of our approach in actual brain stimulation experiments for AD. The main issue that needs to be addressed is replacing the parameters in our model with real values estimated from the analysis of a patient's electrical activity. The selection of the dynamical model used in this work was based on its relative mathematical simplicity (it offers the possibility of assessing both linear and nonlinear cases by switching a single parameter) while still resembling broadly used electro-physiologically-inspired neural mass models[20,54]. Several techniques for estimating its parameters are available, with outstanding results emerging from the use of the innovation method based on local linearization filters[79,80]. However, the estimation of the effective connectivities[12] mediating the interaction between neuronal populations (78×78 values in our case) might constitute a computationally costly problem. This is why, inspired by previous approaches[1,8,9], we focused on the 'structural side' of connectivity for optimally controlling the AD's brain. Both functional and effective connectivity correlate to structural connectivity[13,14].

In this work we assumed that the strength of the structural connectivity was proportional to a measure derived from diffusion MRI tractography –the anatomical connection densities[47]. Nevertheless, there is a consensus on the limited performance of tracking algorithms and anatomically-imposed difficulties that suggests prudence in making such assumption[81]. An inherent limitation of DW-MRI is its inability to detect the direction of nervous fibers[47], which extends to all current neuroimaging methods[11]. However, a substantial proportion of reciprocal connections has been identified[82], justifying the ubiquitous use of undirected anatomical networks. Variability across DW-MRI studies and methods does constitute a major issue to deal with for achieving generalization. For example, there are several definitions of connection weights and normalizations for them[47,83–85], all indistinctively used.

On the other hand, real EEG activity is a mixture of oscillations in different frequency bands, with low-frequency rhythms being spread all over the cortex and high-frequency rhythms being more localized[68]. To assume all nodes in our network oscillate at approximately the same frequency (~6.4 Hz for the 'pathological state', 8.0 Hz for the 'healthy state') is a big approximation. However, given the novelty of our method, this assumption works as a simple approach to provide insights into the optimal stimulation protocols for reverting disease consequences. Our ultimate goal is to design controllers for efficiently and realistically reverting pathological states of each patient's brain.

4.7 Future directions

Our future research intends to use multimodal neuroimaging data to overcome the above-stated imperfections. ADNI is currently registering simultaneous images and working for making this data available (http://adni.loni.usc.edu/study-design/ongoing-investigations/). Estimation

algorithms will likely require further optimization and the use of computing clusters (http://hpc.ucalgary.ca/quickstart/helix) for obtaining the effective connectivities and parameters in the model that produce the activity recorded for each subject. However, once these issues are solved, the framework can be applied to dynamical diseases[86] in general. We have identified Parkinson's[86,87] and epilepsy[8], among others that can be addressed.

In the short term, the possibility of spilling over other brain areas as stimulation focally targets a region, will be studied by using our framework in its current state. Additionally, the intentional stimulation of selected structures with different signals is one modeling alternative that can be associated to faster and less-exposing control of impaired activity. We will assess several combinations of simultaneous stimulations in a separate work.

4.8 Conclusions

In this study, we sought to obtain optimal signals to be used in brain stimulation therapies for AD. Given the knowledge gap between theory and experiment in brain stimulation, as well as the usual neglect of the nonlinear nature of brain dynamics in its modeling, and the need for personalizing treatments in medicine, we started by developing a framework that embodies and solves all these limitations in a simplistic way, by using the so-called state-dependent Riccati equation control.

We used anatomical networks obtained from DW-MRI acquired by ADNI as mediators for the interaction between Duffing-like oscillators. This ensured our modeling approach included both subject-specific information and nonlinearities. Inspired by previous findings of cognitive improvement in AD through EEG abnormalities correction, we looked for control inputs to individual regions of the brain that reverted pathological activity (high-amplitude theta-band

oscillations) at a minimal energetic cost. Considering nonlinearities in our model changed the landscape of optimal network control: signals were intrinsically different from their linear system equivalents, inputs to neuronal populations in certain regions and subjects did not propagate to the rest of the network to accomplish the control objective, and there were changes to the way stimulated regions were ranked in terms of the energetic cost of controlling the entire network. We also obtained insight into the relationship between optimal nonlinear network control and the topological characteristics of anatomical brain networks (better connected means better controlled), and identified top target regions and subjects to successfully undergo our proposed stimulation procedure.

This is the first time, to our knowledge, that optimal nonlinear network control of AD has been addressed. Tailored stimulation signals to control pathological electroencephalographic activity induced by AD were obtained based on individual neuroimaging data and innovative modeling. Additionally, the framework we introduced can be applied to any other clinical condition with associated alterations in brain dynamics, and shed light on both healthy and pathological self-regulatory mechanisms in the brain. Even with limitations in the modeling at this very primary stage of our work and the need of experimental validation, the results herein reported constitute a progress, and overall, this thesis might represent a change to the methodology for addressing the control principles of the brain.

References

1. Muldoon, S. F. *et al.* Stimulation-based control of dynamic brain networks. *PLoS Comput. Biol.* **12,** e1005076 (2016).
2. Laxton, A. W. *et al.* A phase I trial of deep brain stimulation of memory circuits in Alzheimer's disease. *Ann. Neurol.* **68,** 521–534 (2010).
3. Lozano, A. M. *et al.* A Phase II Study of Fornix Deep Brain Stimulation in Mild Alzheimer's Disease. *J. Alzheimer's Dis.* **54,** 777–787 (2016).
4. Rossi, S. *et al.* Safety, ethical considerations, and application guidelines for the use of transcranial magnetic stimulation in clinical practice and research. *Clin. Neurophysiol.* **120,** 2008–2039 (2009).
5. Nitsche, M. A. *et al.* Transcranial direct current stimulation: State of the art 2008. *Brain Stimul.* **1,** 206–223 (2008).
6. Tarsy, D., Vitek, J. L., Starr, P. A. & Okun, M. S. *Deep Brain Stimulation in Neurological and Psychiatric Disorders*. (Humana Press, 2008). doi:10.1007/978-1-59745-360-8
7. Sotero, R. C. & Shmuel, A. Energy-based stochastic control of neural mass models suggests time-varying effective connectivity in the resting state. *J. Comput. Neurosci.* **32,** 563–576 (2012).
8. Taylor, P. N. *et al.* Optimal control based seizure abatement using patient derived connectivity. *Front. Neurosci.* **9,** 1–10 (2015).
9. Betzel, R. F., Gu, S., Medaglia, J. D., Pasqualetti, F. & Bassett, D. S. Optimally controlling the human connectome: the role of network topology. *Sci. Rep.* **6,** 30770 (2016).
10. Bassett, D. S., Khambhati, A. N. & Grafton, S. T. Emerging Frontiers of Neuroengineering:

A Network Science of Brain Connectivity. *Annu. Rev. Biomed. Eng.* **19,** 327–352 (2017).

11. Rubinov, M. & Sporns, O. Complex network measures of brain connectivity: Uses and interpretations. *Neuroimage* **52,** 1059–1069 (2010).
12. Friston, K. Functional and effective connectivity: a review. *Brain Connect.* **1,** 13–36 (2011).
13. Honey, C. J., Thivierge, J. P. & Sporns, O. Can structure predict function in the human brain? *Neuroimage* **52,** 766–776 (2010).
14. Sotero, R. C. *et al.* Anatomically-constrained effective connectivity among layers in a cortical column modeled and estimated from local field potentials. *J. Integr. Neurosci.* **09,** 355–379 (2010).
15. Iturria-Medina, Y., Sotero, R. C., Canales-Rodríguez, E. J., Alemán-Gómez, Y. & Melie-García, L. Studying the human brain anatomical network via diffusion-weighted MRI and Graph Theory. *Neuroimage* **40,** 1064–1076 (2008).
16. Shao, J. *et al.* Prediction of Alzheimer's disease using individual structural connectivity networks. *Neurobiol. Aging* **33,** 2756–2765 (2012).
17. Hendricks, E., Jannerup, O. & Sørense, P. H. *Linear Systems Control*. (Springer Berlin Heidelberg, 2008). doi:10.1007/978-3-540-78486-9
18. Liu, Y.-Y., Slotine, J.-J. & Barabási, A.-L. Controllability of complex networks. *Nature* **473,** 167–73 (2011).
19. Valdes, P. *et al.* The statistical identification of nonlinear brain dynamics: A progress report. *Nov. Sci. Publ.* 278–284 (1999).
20. Valdes-Sosa, P. A. *et al.* Model driven EEG/fMRI fusion of brain oscillations. *Hum. Brain Mapp.* **30,** 2701–2721 (2009).

21. Spiegler, A., Kiebel, S. J., Atay, F. M. & Knösche, T. R. Bifurcation analysis of neural mass models: Impact of extrinsic inputs and dendritic time constants. *Neuroimage* **52,** 1041–1058 (2010).

22. Sotero, R. C. Topology, Cross-Frequency, and Same-Frequency Band Interactions Shape the Generation of Phase-Amplitude Coupling in a Neural Mass Model of a Cortical Column. *PLoS Comput. Biol.* **12,** 1–29 (2016).

23. McKhann, G. M. *et al.* The diagnosis of dementia due to Alzheimer's disease: Recommendations from the National Institute on Aging-Alzheimer's Association workgroups on diagnostic guidelines for Alzheimer's disease. *Alzheimer's Dement.* **7,** 263–269 (2011).

24. Prince, M., Comas-Herrera, A., Knapp, M., Guerchet, M. & Karagiannidou, M. *World Alzheimer Report 2016: improving healthcare for people living with dementia: coverage, quality and costs now and in the future*. (2016).

25. Iturria-Medina, Y., Carbonell, F. M., Sotero, R. C., Chouinard-Decorte, F. & Evans, A. C. Multifactorial causal model of brain (dis)organization and therapeutic intervention: Application to Alzheimer's disease. *Neuroimage* **152,** 60–77 (2017).

26. Iturria-Medina, Y. *et al.* Early role of vascular dysregulation on late-onset Alzheimer's disease based on multifactorial data-driven analysis. *Nat Commun* **7,** 11934 (2016).

27. Bennys, K., Rondouin, G., Vergnes, C. & Touchon, J. Diagnostic value of quantitative EEG in Alzheimer's disease. *Neurophysiol. Clin. Neurophysiol.* **31,** 153–160 (2001).

28. Jeong, J. EEG dynamics in patients with Alzheimer's disease. *Clin. Neurophysiol.* **115,** 1490–1505 (2004).

29. Stam, C. J. in *Niedermeyer's Electroencephalography: Basic Principles, Clinical Applications, and Related Fields* (eds. Schomer, D. L. & Lopes da Silva, F.) 375–393 (Lippincott Williams & Wilkins, 2012).

30. Gianotti, L. R. R. *et al.* Correlation between disease severity and brain electric LORETA tomography in Alzheimer's disease. *Clin. Neurophysiol.* **118,** 186–196 (2007).

31. Adler, G., Brassen, S., Chwalek, K., Dieter, B. & Teufel, M. Prediction of treatment response to rivastigmine in Alzheimer's dementia. *J. Neurol. Neurosurg. Psychiatry* **75,** 292–4 (2004).

32. Lo, C.-Y. *et al.* Diffusion Tensor Tractography Reveals Abnormal Topological Organization in Structural Cortical Networks in Alzheimer's Disease. *J. Neurosci.* **30,** 16876–16885 (2010).

33. Daianu, M. *et al.* Breakdown of Brain Connectivity Between Normal Aging and Alzheimer's Disease: A Structural *k* -Core Network Analysis. *Brain Connect.* **3,** 407–422 (2013).

34. Watts, D. J. & Strogatz, S. H. Collective dynamics of 'small-world' networks. *Nature* **393,** 440–442 (1998).

35. Hsu, W.-Y., Ku, Y., Zanto, T. P. & Gazzaley, A. Effects of noninvasive brain stimulation on cognitive function in healthy aging and Alzheimer's disease: a systematic review and meta-analysis. *Neurobiol. Aging* **36,** 2348–2359 (2015).

36. Wernli, A. & Cook, G. Suboptimal control for the nonlinear quadratic regulator problem. *Automatica* **11,** 75–84 (1975).

37. Çimen, T. State-Dependent Riccati Equation (SDRE) Control: A Survey. *IFAC Proc. Vol.*

41, 3761–3775 (2008).

38. Jayaram, A. & Tadi, M. Synchronization of chaotic systems based on SDRE method. *Chaos, Solitons & Fractals* **28,** 707–715 (2006).

39. Barabási, A.-L. & Albert, R. Emergence of scaling in real world networks. *Science* **286,** 509–512 (1999).

40. Taylor, A. & Higham, D. J. CONTEST: A Controllable Test Matrix Toolbox for MATLAB. *ACM Trans. Math. Softw.* **35,** 1–17 (2009).

41. Batagelj, V. & Brandes, U. Efficient generation of large random networks. *Phys. Rev. E - Stat. Nonlinear, Soft Matter Phys.* **71,** 1–5 (2005).

42. Sled, J. G., Zijdenbos, a P. & Evans, a C. A nonparametric method for automatic correction of intensity nonuniformity in MRI data. *IEEE Trans. Med. Imaging* **17,** 87–97 (1998).

43. Evans, A. C., Kamber, M., Collins, D. L. & MacDonald, D. in *Magnetic Resonance Scanning and Epilepsy* 263–274 (Springer US, 1994). doi:10.1007/978-1-4615-2546-2_48

44. Ashburner, J. A fast diffeomorphic image registration algorithm. *Neuroimage* **38,** 95–113 (2007).

45. Klein, A. & Tourville, J. 101 Labeled Brain Images and a Consistent Human Cortical Labeling Protocol. *Front. Neurosci.* **6,** 1–12 (2012).

46. Studholme, C., Hawkes, D. J. & Hill, D. L. Normalized entropy measure for multimodality image alignment. in *Proc. Medical Imaging* (ed. Hanson, K. M.) 132–143 (SPIEPress, 1998). doi:10.1117/12.310835

47. Iturria-Medina, Y. *et al.* Characterizing brain anatomical connections using diffusion weighted MRI and graph theory. *Neuroimage* **36,** 645–660 (2007).

48. Tournier, J. D. *et al.* Resolving crossing fibres using constrained spherical deconvolution: Validation using diffusion-weighted imaging phantom data. *Neuroimage* **42,** 617–625 (2008).

49. Xia, M., Wang, J. & He, Y. BrainNet Viewer: A Network Visualization Tool for Human Brain Connectomics. *PLoS One* **8,** (2013).

50. Barrat, A., Barthelemy, M., Pastor-Satorras, R. & Vespignani, A. The architecture of complex weighted networks. *Proc. Natl. Acad. Sci.* **101,** 3747–3752 (2004).

51. Estrada, E. & Hatano, N. Communicability in complex networks. *Phys. Rev. E - Stat. Nonlinear, Soft Matter Phys.* **77,** 1–12 (2008).

52. Cloutier, J. R. & Stansbery, D. T. Nonlinear, Hybrid Bank-to-Turn/Skid-to-Turn Missile Autopilot Design. in *AlAA Guidance, Navigation, and Control Conference* **298,** 1–11 (2001).

53. Biscay, R., Jimenez, J. C., Riera, J. J. & Valdes-Sosa, P. A. Local Linearization method for the numerical solution of stochastic differential equations. *Ann. Inst. Stat. Math.* **48,** 631–644 (1996).

54. Sotero, R. C., Trujillo-Barreto, N. J., Iturria-Medina, Y., Carbonell, F. & Jimenez, J. C. Realistically coupled neural mass models can generate EEG rhythms. *Neural Comput.* **19,** 478–512 (2007).

55. Cveticanin, L. in *The Duffing Equation: Nonlinear Oscillators and their Behaviour* 81–137 (John Wiley & Sons, Ltd, 2011). doi:10.1002/9780470977859.ch4

56. Wilson, H. R. & Cowan, J. D. Excitatory and inhibitory interactions in localized populations of model neurons. *Biophys. J.* **12,** 1–24 (1972).

57. Lopes da Silva, F. H., Hoeks, A., Smits, H. & Zetterberg, L. H. Model of brain rhythmic activity. The alpha-rhythm of the thalamus. *Kybernetik* **15,** 27–37 (1974).

58. Jansen, B. H. & Rit, V. G. Electroencephalogram and visual evoked potential generation in a mathematical model of coupled cortical columns. *Biol. Cybern.* **73,** 357–366 (1995).

59. David, O. & Friston, K. J. A neural mass model for MEG/EEG: Coupling and neuronal dynamics. *Neuroimage* **20,** 1743–1755 (2003).

60. Kawahara, T. Coupled Van der Pol oscillators - A model of excitatory and inhibitory neural interactions. *Biol. Cybern.* **39,** 37–43 (1980).

61. Zavaglia, M., Astolfi, L., Babiloni, F. & Ursino, M. A neural mass model for the simulation of cortical activity estimated from high resolution EEG during cognitive or motor tasks. *J. Neurosci. Methods* **157,** 317–329 (2006).

62. Schork, N. J. Personalized medicine: Time for one-person trials. *Nature* **520,** 609–611 (2015).

63. Tang, E. & Bassett, D. S. Control of Dynamics in Brain Networks. *arXiv Prepr.* (2017).

64. Latora, V. & Marchiori, M. Efficient Behavior of Small-World Networks. 3–6 (2001). doi:10.1103/PhysRevLett.87.198701

65. Morgane, P., Galler, J. & Mokler, D. A review of systems and networks of the limbic forebrain/limbic midbrain. *Prog. Neurobiol.* **75,** 143–160 (2005).

66. Lanciego, J. L., Luquin, N. & Obeso, J. A. Functional neuroanatomy of the basal ganglia. *Cold Spring Harb. Perspect. Med.* **2,** 1–20 (2012).

67. Mišić, B., Goñi, J., Betzel, R. F., Sporns, O. & McIntosh, A. R. A Network Convergence Zone in the Hippocampus. *PLoS Comput. Biol.* **10,** (2014).

68. Canolty, R. T. & Knight, R. T. The functional role of cross-frequency coupling. *Trends Cogn. Sci.* **14,** 506–515 (2010).

69. Bickart, K. C. *et al.* The amygdala as a hub in brain networks that support social life. *Neuropsychologia* **63,** 235–248 (2014).

70. Giannakopoulos, P., Kovari, E., Herrmann, F. R., Hof, P. R. & Bouras, C. Interhemispheric Distribution of Alzheimer Disease and Vascular Pathology in Brain Aging. *Stroke* **40,** 983–986 (2009).

71. Grossman, N. *et al.* Noninvasive Deep Brain Stimulation via Temporally Interfering Electric Fields. *Cell* **169,** 1029–1041.e16 (2017).

72. Terney, D., Chaieb, L., Moliadze, V., Antal, A. & Paulus, W. Increasing Human Brain Excitability by Transcranial High-Frequency Random Noise Stimulation. *J. Neurosci.* **28,** 14147–14155 (2008).

73. Butson, C. R. & McIntyre, C. C. Role of electrode design on the volume of tissue activated during deep brain stimulation. *J. Neural Eng.* **3,** 1–8 (2006).

74. Woods, A. J. *et al.* A technical guide to tDCS, and related non-invasive brain stimulation tools. *Clin. Neurophysiol.* **127,** 1031–1048 (2016).

75. Little, S. *et al.* Adaptive deep brain stimulation in advanced Parkinson disease. *Ann. Neurol.* **74,** 449–457 (2013).

76. Little, S. *et al.* Bilateral adaptive deep brain stimulation is effective in Parkinson's disease. *J. Neurol. Neurosurg. Psychiatry* **87,** 717–721 (2016).

77. Rosa, M. *et al.* Adaptive deep brain stimulation in a freely moving parkinsonian patient. *Mov. Disord.* **30,** 1003–1005 (2015).

78. Rosa, M. *et al.* Adaptive deep brain stimulation controls levodopa-induced side effects in Parkinsonian patients. *Mov. Disord.* **32,** 628–629 (2017).

79. Jimenez, J. C. & Ozaki, T. An approximate innovation method for the estimation of diffusion processes from discrete data. *J. Time Ser. Anal.* **27,** 77–97 (2005).

80. Sotero, R. C., Trujillo-Barreto, N. J., Jiménez, J. C., Carbonell, F. & Rodríguez-Rojas, R. Identification and comparison of stochastic metabolic/hemodynamic models (sMHM) for the generation of the BOLD signal. *J. Comput. Neurosci.* **26,** 251–269 (2009).

81. Jones, D. K., Knösche, T. R. & Turner, R. White matter integrity, fiber count, and other fallacies: The do's and don'ts of diffusion MRI. *Neuroimage* **73,** 239–254 (2013).

82. Young, M. P. The organization of neural systems in the primate cerebral cortex. *Proc.r.soc.l. B Biol.Sci.* **252,** 13–18 (1993).

83. Hagmann, P. *et al.* Mapping human whole-brain structural networks with diffusion MRI. *PLoS One* **2,** (2007).

84. Bassett, D. S., Brown, J. A., Deshpande, V., Carlson, J. M. & Grafton, S. T. Conserved and variable architecture of human white matter connectivity. *Neuroimage* **54,** 1262–1279 (2011).

85. Duarte-Carvajalino, J. M. *et al.* Hierarchical topological network analysis of anatomical human brain connectivity and differences related to sex and kinship. *Neuroimage* **59,** 3784–3804 (2012).

86. Schiff, S. J. Towards model-based control of Parkinson's disease. *Philos. Trans. R. Soc. A Math. Phys. Eng. Sci.* **368,** 2269–2308 (2010).

87. Rubin, J. E. & Terman, D. High Frequency Stimulation of the Subthalamic Nucleus

Eliminates Pathological Thalamic Rhythmicity in a Computational Model. *J. Comput. Neurosci.* **16,** 211–235 (2004).

88. Kringelbach, M. L., Jenkinson, N., Owen, S. L. F. & Aziz, T. Z. Translational principles of deep brain stimulation. *Nat. Rev. Neurosci.* **8,** 623–635 (2007).

89. Liu, Y.-Y., Slotine, J.-J. & Barabási, A.-L. Controllability of complex networks (Supplementary material). *Nature* **473,** 167–73 (2011).

```
function
NLduff_ADNI_hd_subject(subject,b,ah,ad,Qweight,g,node)
%   NLDUFF_ADNI_HD_SUBJECT(SUBJECT,B,AH,AD,QWEIGHT,G,NODE)
%   creates a file containing the results of controlling
the pathological
%   activity of a AD-subject from a given node
%
%   This function will generate two solutions, a
pathological EEG (expected
%   to be a theta rhythm) and healthy EEG (alpha rhythm).
The initial
%   conditions are set for the pathological solution have
higher amplitude
%   and, consequently, more spectral power (see, e.g.,
Bennys 2001). Then,
%   the optimal input that reverts the pathological
activity in the
%   nonlinear system is computed (see Cimen 2008; Jayaram &
Tadi 2006). The
%   difference between the pathological (Z) and healthy
solutions (X),
%   e = Z - X goes to the equilibrium
%
%   Inputs:
%   subject: Subject's ID according to ADNI's database
(adni.loni.usc.edu)
%   b: Global coupling strength
%   ah: 'Time constant' for the computation of the
'healthy' solution
%   ad: 'Time constant' for the computation of the
'pathological' solution
%   Qweight: weight on the cost function for the separation
of the states
%            from the equilibrium
%   g: Strength of the nonlinearity
%   node: index corresponding to the node that receives the
input
%
%   Notes:
```

```
%   - All the inputs must be string arrays
%   - The file Conn_matrices_backbone.mat contains the
network backbone,
%   with the dominant connections in the average network.
The file AD_DTI.mat
%   summarized demographic information of the subjects in
the study
%   (including their ID's - this is how the networks are
tagged) and the
%   anatomical networks calculated from DW-MRI for each
subject in ADNI by
%   Yasser Iturria-Medina. (see, e.g., Iturria-Medina et
al. 2017)
%   - The non-feedback system is defined in the auxiliary
function
%   F_Duffing_simplecoupling_1Dpars and solved with
MATLAB's ode45
%   - The feedback system is solved following:
%   1) solve SDRE with MATLAB's lqr, obtain K
%   2) use that the optimal input is u = -R^(-1)*B'*S*e = -
K*e (see Cimen 2008)
%   3) obtain the next iteration's e by using Local
Linearization
%   (see, e.g., Biscay et al. 1996)
%   - Controlling a linear system can be studied by means
of this same
%   function, making g = 0.
%
%   example:
NLduff_ADNI_healthydis_subject('5119','150','2852','1935','
1','200','37')

%  converting the inputs to double
Qweight = str2double(Qweight);
b = str2double(b);
g = str2double(g);
node = str2double(node);
ah = str2double(ah);
ad = str2double(ad);
subject = str2double(subject);
d = 0;
```

```
% loading the connection network for the desired subject
type = 'AD';
load('Conn_matrices_backbone.mat')
load('AD_DTI.mat')
AD_ids_all = cell2mat(demog_AD(:,1));
subject_idx = find(AD_ids_all == subject);
C = AD_conn_ACD(1:78,1:78,subject_idx).*Matrix_backbone;

% definitions for calculating
N = length(C);
X0 = [0.1*ones(1,N),zeros(1,N)];
Z0 = [0.2*ones(1,N),zeros(1,N)];
dt = 0.01;
t = 0:dt:500;

% obtain the healthy solution
thetah = cat(2,d,ah,g,b);
options = odeset('RelTol',1e-6,'AbsTol',1e-6);
[~, X] =
ode45(@F_Duffing_simplecoupling_1Dpars,t,X0,options,thetah,
C);
% obtain the pathological solution
thetad = cat(2,d,ad,g,b);
options = odeset('RelTol',1e-6,'AbsTol',1e-6);
[~, Z] =
ode45(@F_Duffing_simplecoupling_1Dpars,t,Z0,options,thetad,
C);

% the difference between the two solutions before
controlling (for comparison)
e_nocont = Z - X;

% constructing control matrices
A = zeros(2*N+1); A(1:N,N+1:2*N) = eye(N);
A(N+1:2*N,N+1:2*N) = -diag(d);
A(end,end) = -1;
B = zeros(2*N+1,1);B(N+node) = 1e2;
Q = Qweight*eye(N); Q(2*N+1,2*N+1) = 0;
R= 1;
Nt = length(t);
```

```
% calculating
u = zeros(Nt,1);
Cost = zeros(Nt,1);
Cost_u = zeros(Nt,1);
e = zeros(Nt,2*N+1);
e(1,:) = [(Z0 - X0)';1];
S_JC = zeros(2*N+1,1);
for tf = 1:1:Nt-1

    elocal = e(tf,:)';
    Acool = diag(b)*C;
    Acool(eye(N)~=0)= -ad - g.*(elocal(1:N)'.^2 +
3*elocal(1:N)'.*X(tf,1:N) + 3*X(tf,1:N).^2);
    A(N+1:2*N,1:N) = Acool;
    A(N+1:2*N,end) = -(ad-ah).*X(tf,1:N);

    try
        K=lqr(A,B,Q,R);
    catch
        save(sprintf('ADNI_%s_%i_%i-
Cont_Q=%i_R=%i_GlobCoup=%.2f_g=%.1f_ah=%i_ad=%i_FAILED.mat'
,type,subject,node,Qweight,R(1,1),b,g,ah,ad));
        return
    end

    u(tf) = -K*elocal;
    Cost(tf) = elocal'*Q*elocal + u(tf,:)*R*u(tf,:)';
    Cost_u(tf) = u(tf,:)*R*u(tf,:)';

    fe = f_duff_LL(elocal,A,B,K);
    Jfxe = Jfx_duff_LL(elocal,A,B,K);
    e(tf+1,:) = elocal + DLLscheme_JC(dt,fe,Jfxe,S_JC);

end
efinal = e(end,:)';
Acool(eye(N)~=0)= -ad - g.*(efinal(1:N)'.^2 +
3*efinal(1:N)'.*X(tf,1:N) + 3*X(tf,1:N).^2); A(N+1:2*N,1:N)
= Acool;
Kfinal=lqr(A,B,Q,R);
u(end,:) = -Kfinal*efinal;
```

```
Cost(end) = efinal'*Q*efinal + u(end,:)*R*u(end,:)';
Cost_u(end) = u(end,:)*R*u(end,:)';

% obtaining the cost of controlling
totCost = trapz(t,Cost);
totCost_u = trapz(t,Cost_u); % (part corresponding to the
energy used by the controller)

%saving results
save(sprintf('ADNI_%s_%i_%i-
Cont_Q=%i_R=%i_GlobCoup=%.2f_g=%.1f_ah=%i_ad=%i.mat',type,s
ubject,node,Qweight,R(1,1),b,g,ah,ad),'C','Qweight','Q','R'
,'t','X0','Z0',...

'X','Z','u','e','e_nocont','totCost','totCost_u','norm_xx',
'controlled_LL','-v7.3');


function f = F_Duffing_simplecoupling_1Dpars(t,x,theta,C)
N = length(x)/2;
d = theta(1);
a = theta(2);
g = theta(3);
b = theta(4);
f = zeros(2*N,1);
f(1:N) = x(N+1:end);
for i = 1:N
    f(i+N) = -d*x(i+N) - a*x(i) - g*x(i)^3 +
b*sum(C(:,i).*x(1:N));
end

function y = DLLscheme_JC(h,f,fx,ft)
n=size(f,1);
CC=[fx, ft, f; zeros(2,n+2)];
CC(n+1,n+2)=1;
M=expm(h*CC);
y=M(1:n,n+2);

function f = f_duff_LL(x,A,B,K)
f = (A - B*K)*x;
```

```
function Jfx = Jfx_duff_LL(x,A,B,K)
Jfx = A - B*K;
```